

1 **Initiating Photocatalytic Degradation of Organic Pollutants under**
2 **Ultra-Low Light Intensity via Oxygen-Centered Organic Radicals**

3 Yingge He^a, Yuyan Huang^b, Yu-Xin Ye^{c,d*}, Yanchun Deng^a, Xin Yang^{a*}, Gangfeng Ouyang^{b,c,d*}

4 ^aSchool of Environmental Science and Engineering, Guangdong Provincial Key Laboratory of
5 Environmental Pollution Control and Remediation Technology, Sun Yat-sen University,
6 Guangzhou, China.

7 ^bKey Laboratory of Bioinorganic and Synthetic Chemistry of Ministry of Education, LIFM,
8 School of Chemistry, IGCME, Sun Yat-Sen University, Guangzhou, China.

9 ^cSchool of Chemical Engineering and Technology, IGCME, Sun Yat-sen University, Zhuhai,
10 China.

11 ^dSouthern Marine Science and Engineering Guangdong Laboratory (Zhuhai), Zhuhai, China.

12 *Correspondence to: yeyuxin5@sysu.edu.cn; yangx36@mail.sysu.edu.cn; cesoygf@mail.sysu.edu.cn
13 du.cn

14

15

Table of contents

16	Supplemental Methods	4
17	Materials	4
18	Synthesis of TPE-AQ-molecule	5
19	Characterization	5
20	Photocatalytic Experiments	6
21	Electrochemical measurements	7
22	EPR Analysis	8
23	Recycling Experiments	10
24	Determination of H ₂ O ₂ concentration	10
25	Evaluation of KIE (Kinetic Isotope Effect)	11
26	Analytical methods	11
27	Supplemental Notes	13
28	Supplemental Note 1. Charge carriers separation and transfer performance of CPs	
29	13
30	Supplemental Note 2. Attribution of signals in transient absorption spectra	13
31	Supplemental Figures	15
32	Figure S1. PXRD patterns of TPE-AQ and TPE-FN.	15
33	Figure S2. Scanning electron microscope (SEM) images of CPs.	16
34	Figure S3. FT-IR spectra of TPE-AQ, TPE-FN, and monomer.	17
35	Figure S4. The XPS spectra of TPE-AQ and TPE-FN.	18
36	Figure S5. Solid state ¹³ C CP-MAS NMR spectra.	19
37	Figure S6. Measurements of Brunauer-Emmett-Teller surface areas.	20
38	Figure S7. Characterization of CBM through Mott Schottky.	21
39	Figure S8. XPS valence band spectrum of CPs.	22
40	Figure S9. Characterization of sample work function through Kelvin Probe Force	
41	Microscopy (KPFM).	23
42	Figure S10. Solar irradiance levels under various environmental conditions.	24
43	Figure S11. The experimental device and light source spectrum.	25
44	Figure S12. Reaction condition gradient experiments.	26

45	Figure S13. The photocatalytic performance of CPs for BPA degradation.	27
46	Figure S14. The withstand interference ability test.	28
47	Figure S15. Recycle experiments of TPE-AQ.	29
48	Figure S16. Post-characterization of TPE-AQ after photocatalysis.	30
49	Figure S17. Degradation of different micropollutants in the TPE-AQ system. ...	31
50	Figure S18. EPR spectra of TPE-AQ.	32
51	Figure S19. Photoluminescence spectra of TPE-AQ, TPE-FN, and	
52	TPE-AQ-molecule.	33
53	Figure S20. Photocurrent responses and electrochemical impedance spectroscopy	
54	analysis.	34
55	Figure S21. Femtosecond transient absorption measurements probed at visible	
56	region.	35
57	Figure S22. Δ EPR signal intensity as a function of excitation wavelength.	36
58	Figure S23. The lifetime of OCORs.	37
59	Figure S24. Femtosecond transient absorption measurements probed at	
60	near-infrared region.	38
61	Figure S25. The time-dependent in-situ EPR spectra of TPE-AQ in H ₂ O.	39
62	Figure S26. Characterization of the electron storage properties of TPE-AQ.	40
63	Figure S27. H/D kinetic isotope effect for phenol degradation in TPE-AQ system	
64	41
65	Figure S28. Photocatalytic degradation pathway of BPA.	42
66	Figure S29. TOC removal in the TPE-AQ system.	43
67	Figure S30. Effect of atmospheric on the photocatalytic performance of TPE-AQ.	
68	44
69	Supplemental Tables	45
70	Table S1. Photocatalytic activity and light intensity between TPE-AQ and other	
71	reported photocatalysts for micropollutants degradation.	45
72	Table S2. The HPLC conditions for analysis of different micropollutants.	46
73	Table S3. Atomic coordinates of the TPE-AQ optimized computational model. .	47
74	Table S4. Atomic coordinates of the TPE-FN optimized computational model. .	49

75	Table S5. Time-dependent density functional theory (TD-DFT) of TPE-AQ and	
76	TPE-FN.	51
77	Table S6. Water quality parameters of the actual water.	52
78	Table S7. Summary of the half-life and redox potential of common transient	
79	active species and OCORs.	53
80	Table S8. Single-point energy of each substance.	54
81	Table S9. Identification of transformation products of BPA in the TPE-AQ system.	
82	56
83	Table S10. Baseline toxicity data predicted using the ECOSAR program of EPI	
84	Suite 4.0.	57
85	Supplemental References	59
86		
87		

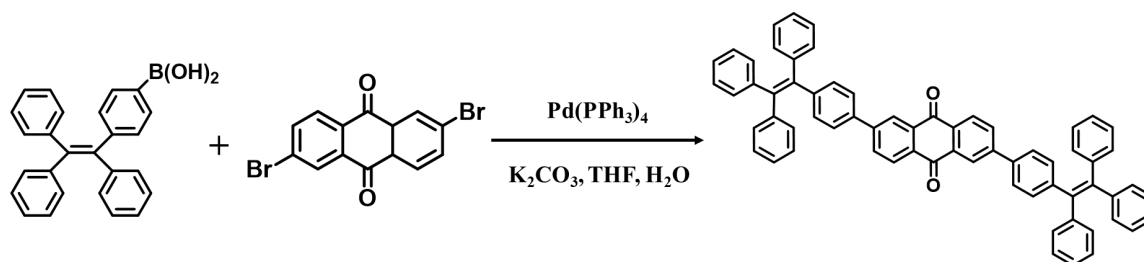
88 **Supplemental Methods**

89 **Materials**

90 2,6-dibromoanthraquinone (96%) and potassium carbonate (K_2CO_3 , 99%) were purchased from
91 Bidepharm (Shanghai, China). [ethene-1,1,2,2-tetrayltetrakis(benzene-4,1-diyl)]tetraboronic acid
92 (>95%) was purchased from Jilin Chinese Academy of Sciences-Yanshen Technology.
93 [4-(1,2,2-triphenylethenyl)phenyl]boronic acid (97%) was purchased from Shanghai Tensus
94 Biotech Co., Ltd. Tetrakis(triphenylphosphine)palladium ($Pd(PPh_3)_4$, 99%) was obtained from
95 Energy Chemical. TCI supplied the 2,7-dibromo-9-fluorenone (>98%). Phenol (99.5%),
96 p-chlorophenol (4-CP, 99.5%), and superoxide dismutase (SOD, 20000 units/mg) were purchased
97 from Macklin Biochemical Co., Ltd (Shanghai, China). 5,5-dimethyl-1-pyrroline N-oxide (DMPO,
98 98%), 2,2,6,6-tetramethyl-4-piperidinol (TEMP, 98%), bisphenol A (BPA, 98%), sulfamethoxazole
99 (SMX, 98%), carbamazepine (CBZ, 99%), aniline (98%), triclosan (TCS, 98%), deferoxamine
100 mesylate salt (DFO), L-histidine (99%) and N, N-dimethylformamide (DMF, 99.8%) were
101 purchased from Sigma-Aldrich. Catalase from bovine liver (3000 units/mg) was purchased from
102 Lounbiotech (Guangzhou, China). Silver nitrate ($AgNO_3$) and ethylenediaminetetraacetic acid
103 disodium salt (EDTA-2Na) were obtained from the Guangzhou Chemical Reagent Factory.
104 Tert-butyl alcohol (TBA) was supplied by ANPLE Laboratory Technologies (China). Suwannee
105 River Natural Organic Matter (SRNOM, 2S101N) was obtained from the International Humic
106 Substances Society (IHSS). The actual water samples (Beijiang River, Xiaogu River, and Sea
107 water) were all filtered with 0.45 μm filter membrane and kept in the dark at 4 °C until use. The
108 basic characteristics of the actual water were collected in Table S4. All materials were used as
109 received without further purification or treatment. Ultrapure water (>18 $M\Omega \cdot cm$) was used for all

110 the experiments.

111 Synthesis of TPE-AQ-molecule



TPE-AQ-molecule

112

113 Into a three-necked flask, [4-(1,2,2-triphenylethenyl)phenyl]boronic acid (90.30 mg, 0.24 mmol),

114 2,6-dibromoanthraquinone (36.60 mg, 0.1 mmol), Pd(PPh₃)₄ (2.68 mg, 0.0023 mmol), K₂CO₃ (20

115 mg, 0.14 mmol), and a mixed solvent of THF/H₂O (15 mL/3 mL, respectively) were added. The

116 system was purged with argon gas for 30 minutes. Then, the mixture was heated to 80 °C and

117 stirred overnight. After cooling down to room temperature, water was added, and the mixture was

118 extracted with DCM. The organic phase was collected. Following solvent evaporation, the residue

119 was purified by column chromatography on silica gel (55% yield). ¹H-NMR (400 MHz,

120 Chloroform-d): δ 8.52 ppm (d, J = 1.9 Hz, 2H), 8.37 (d, J = 8.2 Hz, 2H), 8.00 (m, 2H), 7.52 (d, J =

121 8.2 Hz, 4H), 7.21-7.11 (m, 34H).

122 Characterization

123 The sample's morphology was examined using a high-resolution field-emission scanning electron

124 microscope (FE-SEM, Hitachi SU8010, Japan) at a 10 kV accelerating voltage. Transmission

125 electron microscope (TEM) observation was carried out using JEOL JEM-ARM200P. The

126 crystalline phases were characterized by a powder X-ray diffraction instrument (D-MAX 2200

127 VPC) and the diffractometer was operated at 40 kV and 26 mA and scanned at 10° min⁻¹ from 10°

128 to 80°. X-ray photoelectron spectroscopy (XPS) measurements were recorded by using a Thermo

129 Scientific K-Alpha spectrometer with Al K α radiation as the excitation source. Fourier transform
130 infrared spectra (FT-IR) was recorded on a PerkinElmer Frontier spectrometer. UV-visible
131 spectroscopy (UV-Vis) was carried out on a Shimadzu UV-3600 spectrometer. ¹H NMR spectra
132 were recorded on Bruker advance III 400 MHz. The solid-state ¹³C NMR spectra were performed
133 on Bruker Ascend 600 MHz. Electron paramagnetic resonance (EPR) signals were recorded by
134 Bruker EMXplus. Atomic force microscopy (AFM) measurements were carried out by using the
135 Bruker dimension icon. Photoluminescence (PL) spectra were recorded on an FLS 1000
136 spectrometer. N₂ isotherms and surface area measurements were performed on a JW-BK200C
137 instrument.

138 **Photocatalytic Experiments**

139 In this work, photo-degradation of micropollutants under weak visible light irradiation was
140 employed to evaluate the photocatalytic performance of catalysts. 2.5 mg of photocatalysts were
141 added to 50 mL of ultrapure water in a 50 mL beaker. The catalyst was dispersed by vortex for 30
142 minutes and irradiated by a conventional lamp tube under magnetic stirring. The light intensity on
143 the reaction interface was set to 2.0 mW cm⁻² except for the light intensity gradient experiment,
144 which was measured with a solar power meter (Tenmars, TM-207). 1.0 mL of suspension solution
145 was taken out during irradiation and filtered by 0.45 μ m PTFE hydrophilic filter at predefined
146 time intervals. Then the solution was desorbed in acetonitrile to determine the percentage of
147 adsorption and degradation in the removal of bisphenol A (BPA), the sampling method was the
148 same as mentioned above. Other micropollutants degradation was performed in a similar way as
149 BPA except that they reacted in darkness for 120 minutes before irradiation to achieve
150 adsorption-desorption equilibrium.

151 The radical scavengers quenching experiments were performed using 10 mM silver nitrate
152 (AgNO_3), ethylenediaminetetraacetic acid disodium salt (EDTA-2Na), tert-butyl alcohol (TBA),
153 and L-histidine to quench electrons, holes, $\cdot\text{OH}$, and $^1\text{O}_2$, respectively. 50 U mL^{-1} superoxide
154 dismutase (SOD) and catalase were used as quenchers for $\text{O}_2^{\cdot-}$ and H_2O_2 , respectively. The
155 quenchers were added before the reaction began and other conditions remained the same. For
156 deferoxamine mesylate salt (DFO), a semiquinone free radical quencher was added after the
157 solution reaction in the dark for 30 minutes to ensure that DFO would not affect the adsorption of
158 BPA.

159 For the control experiment under an oxygen/argon atmosphere, the reaction solutions were
160 bubbled with O_2/Ar for 30 minutes before the reaction began, and oxygen or argon gas was
161 continuously bubbled into the system during the experiment. Other conditions remain the same.

162 Each group of experiments was repeated twice to ensure the repeatability and accuracy of the
163 experiment. The results were expressed as average values with error bars displaying the standard
164 deviation.

165 **Electrochemical measurements**

166 All measurements were carried out using an electrochemical workstation (CHI 660E Instruments
167 or CHI 760E Instruments). A three-electrode cell system was employed including an Ag/AgCl
168 reference electrode, a counter electrode of Pt foil, and a working electrode. A 300 W Xe lamp ($\lambda >$
169 400 nm) was used as an illumination source and adjusted the light source distance so that the light
170 intensity was 20-30 mW cm^{-2} .

171 For the photocurrent measurement, the FTO glass (1×1 cm) deposited with materials was used as
172 photoelectrode. The three electrodes were inserted in a quartz cell filled with 0.1 M Na_2SO_4 .

173 During the test, the system was purged with N₂. 0.5 M Na₂SO₄ was used as the electrolyte for the
174 EIS and Mot-Schottky curve. Glassy carbon electrodes and FTO glass (1 × 1 cm) deposited with
175 materials were used as photoelectrode, respectively. CV measurement was conducted in 0.1 M
176 KCl at a sweep rate of 50 mV s⁻¹. Glassy carbon electrodes deposited with materials were used as
177 photoelectrode and the voltage was swept from -1 V to 1.8 V (vs Ag/AgCl).

178 All materials were prepared by adding 2 mg catalyst into the solution containing 180 μL ethanol
179 and 20 μL 5% Nafion. The mixture was dispersed by ultrasonication.

180 **EPR Analysis**

181 **In-situ EPR to monitor the reaction between OCORs and BPA**

182 EPR was used to explore the role of OCORs in the photocatalytic degradation of BPA. A certain
183 amount of material solution was drawn up in a capillary tube, transferred to a quartz tube, and
184 placed in the sample chamber. The EPR signal was initially recorded in the dark, then the BPA
185 solution was added and the material solution was continuously illuminated. The EPR signals were
186 recorded at regular intervals.

187 The materials solution was prepared by adding 10 mg catalysts into 0.1 mL ultrapure water and
188 dispersed by ultrasonication.

189 **The relationship between OCORs concentration and excitation wavelength and excitation** 190 **light intensity**

191 The relation between OCORs concentration and excitation wavelength and excitation light
192 intensity was investigated using EPR. A certain amount of material solution was drawn up in a
193 capillary tube, transferred to a quartz tube, and placed in the sample chamber. The EPR signal was
194 recorded at room temperature without additional light source as control, then the EPR signal was

195 measured after irradiating the material solution for 60 s at different excitation wavelengths and
196 excitation light intensities. The relationship between EPR signal increase and excitation light and
197 excitation wavelength was compared.

198 The materials solution was prepared by adding 10 mg TPE-AQ into 0.1 mL ultrapure water and
199 dispersed by ultrasonication.

200 **Oxygen-centered organic radicals (OCORs) lifetime**

201 In-situ EPR was used to record the signals of OCORs and their lifetimes. For the solid EPR test,
202 20 mg of materials were directly weighed into the quartz tube and placed in the sample chamber.
203 The EPR signals were originally recorded in dark conditions. Following that, the signals were
204 monitored under continuous in-situ irradiation with a conventional lamp tube, and the signal
205 changes were recorded at intervals of irradiation. After 30 minutes of irradiation, the changes in
206 OCORs concentration were tracked by monitoring the signal intensity changes after the light
207 source was removed.

208 For the test of TPE-AQ lifetime in water, a certain amount of material solution was drawn up in a
209 capillary tube, transferred to a quartz tube, and placed in the sample chamber. The test method was
210 the same as the solid in-situ EPR, and the TPE-AQ solution was prepared following the same steps
211 as described earlier.

212 **The electron storage characteristic in TPE-AQ**

213 EPR was used to investigate the electron storage characteristic in TPE-AQ. A certain amount of
214 material solution was drawn up in a capillary tube, placed into a quartz tube, and inserted into the
215 sample chamber. The EPR signal was originally recorded in the dark. Then the solution was
216 illuminated for 30 minutes and tested. Following that, the light source was turned off and 0.01 mL

217 of phenol solution (0.5 M) was added, the reaction was darkened for 30 minutes and examined.
218 The variations in the EPR signal of blank, light for 30 minutes, and reaction in dark with or
219 without phenol for 30 minutes were compared.

220 The preparation of the catalyst solution followed the same steps as described earlier.

221 **Detect of transient reactive Species ($\cdot\text{OH}$, $\text{O}_2^{\cdot-}$, $^1\text{O}_2$)**

222 To examine the reactive species in the photocatalytic process, 5,5-dimethyl-1-pyrroline-N-oxide
223 (DMPO) was used as a trapping agent to detect DMPO- $\cdot\text{OH}$ and DMPO- $\text{O}_2^{\cdot-}$ adducts in aqueous
224 solution and methanol, respectively. 2,2,6,6-tetramethylpiperidine (TEMP) was employed as the
225 spin capture reagent to detect the $^1\text{O}_2$ in an aqueous solution. A conventional lamp tube was used
226 to provide the light source. After irradiation for a certain time, 0.5 mL of the reaction liquid was
227 filtered and added into a centrifuge tube containing the trapping agent and mixed, then the
228 appropriate amount of the mixture was drawn up in a capillary tube, placed into a quartz tube and
229 inserted into the sample chamber, the spectra were recorded.

230 **Recycling Experiments**

231 TPE-AQ recycling studies were carried out as follows: Suction filtering was used to separate the
232 TPE-AQ from the desorption solution after a photocatalytic cycle. After washing with ethanol, the
233 residual catalyst was dried at 80 °C and collected for the next recycling test.

234 **Determination of H_2O_2 concentration**

235 The amount of H_2O_2 was measured using a TMB- H_2O_2 -HRP enzymatic assay, and the horseradish
236 peroxidase (HRP) could catalyze the reaction between H_2O_2 and TMB:



237 The 3,3',5,5'-tetramethylbenzidine (TMB) solution was prepared as follows: 0.015 g TMB was

238 dissolved in 0.3 mL of DMSO, then adding 5 mL of glycerol and 45 mL of ultrapure water
239 containing 0.02 g of ethylenediaminetetraacetic acid and 0.095 g of citric acid. Then the solution
240 was filled to 500 mL with ultrapure water.

241 HRP solution was made by dissolving 0.002 g of peroxidase (from horseradish) in 10 mL of
242 ultrapure water.

243 The calibration curve was determined in the following method: TMB and HRP were added to a
244 known concentration of H₂O₂ solution. After 3 minutes, 10 μL of HCl was added to quench the
245 reaction, and the results were analyzed using UV-visible spectroscopy at 450 nm. The H₂O₂
246 concentration of the samples could be calculated using the linear relationship between signal
247 intensity and H₂O₂ concentration.

248 **Evaluation of KIE (Kinetic Isotope Effect)**

249 The reaction rate was evaluated by a pseudo-first-order kinetics model:

$$250 \qquad \qquad \qquad \ln(C_t/C_0) = -k_{\text{obs}}t \qquad \qquad \qquad (1)$$

251 Where C₀ was the pollutant concentration after adsorption, and C_t was the concentration at a
252 certain time during the photocatalytic degradation process.

253 The KIE equation was as follows:

$$254 \qquad \qquad \qquad \text{KIE} = k_{\text{obs(H)}}/k_{\text{obs(D)}} \qquad \qquad \qquad (2)$$

255 Where the k_{obs(H)} and k_{obs(D)} were the kinetic rate constants of phenol and phenol-D6 degradation,
256 respectively.

257 **Analytical methods**

258 Micropollutant concentrations were determined using high-performance liquid chromatography
259 (HPLC, UltiMate TM 3000, Thermo Fisher Scientific Inc., USA). Chromatographic separation

260 was performed on a CNW Athena C18-WP column (4.6×150 mm, $5 \mu\text{m}$), and the HPLC method
261 for each micropollutant was shown in Table S2. The concentration of the total organic carbon
262 (TOC) in the filtered reaction solution was measured using a TOC analyzer (TOC-L CPH,
263 Shimadzu, Japan). Ultrahigh-performance liquid chromatography coupled with trapped ion
264 mobility time-of-flight mass spectrometer (UltiMate3000-tims TOF) was used for the
265 identification of BPA degradation products, the test method of ion mobility Q-TOF high resolution
266 liquid chromatography mass spectrometry is as follows: Mobile phase A is 0.1% formic acid water,
267 mobile phase B is 0.1% formic acid acetonitrile solution, and the gradient is set as 90% mobile
268 phase A and 10% mobile phase B at 0-1 min, and 5% mobile phase A and 95% mobile phase B at
269 9.5 min and maintained until 12 min. At 12.1 minutes, 90% mobile phase A and 10% mobile phase
270 B were maintained for 15 min with a flow rate of 0.3 mL min^{-1} . ESI negative ion and positive ion
271 modes were used for mass spectrum scanning. The ion source temperature was $120 \text{ }^\circ\text{C}$, the
272 capillary voltage was 2500 V, the cone hole voltage was 35 V, the desolvation temperature was
273 $300 \text{ }^\circ\text{C}$, the cone hole gas flow rate was 40 L h^{-1} , the desolvation gas flow rate is 700 L
274 h^{-1} (negative ion mode) and 750 L h^{-1} (positive ion mode), the nebuliser gas flow rate is 6.5 bar, the
275 trap collision energy is 4.0 eV, and the scanning mass range is 50-1000 Da.

276

277 **Supplemental Notes**

278 **Supplemental Note 1. Charge carriers separation and transfer performance of CPs**

279 The overall recombination efficiencies of photo-induced carriers were monitored by steady-state
280 photoluminescence (PL) emission spectroscopy (Figure S19). The PL intensity was negligible in
281 TPE-AQ, while it was still significant in TPE-FN and TPE-AQ-molecule, indicating the highly
282 improved the separation efficiency of photo-induced carriers in TPE-AQ. Temperature-dependent
283 photoluminescence (PL) spectra were recorded to further elucidate the charge recombination and
284 separation kinetics of CPs (Figs. 4d, e). Clearly, TPE-AQ and TPE-FN exhibited the thermal
285 quenching phenomenon of PL emission in the temperature range from 125 to 300 K. By fitting the
286 PL intensities as a function of temperature using the Arrhenius equation (equation S3), the exciton
287 activation energy (E_a) of TPE-AQ and TPE-FN could be deduced as 158 and 200 meV,
288 respectively¹. The lower E_a implied better charge separation in TPE-AQ.

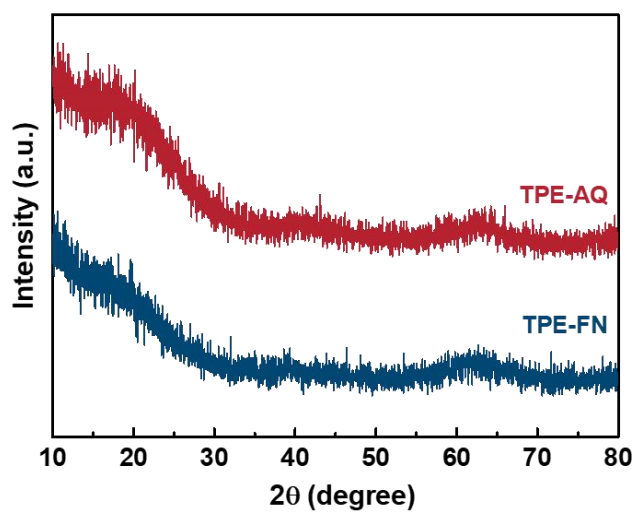
$$289 \quad I(T) = I_0 / (1 + A \exp(-E_b/k_b T)) \quad (3)$$

290 Moreover, photoelectrochemical characterizations provided further significant evidence (Figure
291 S20). The photocurrent experimental results revealed that TPE-AQ displayed a higher
292 photocurrent response, signifying less recombination and faster photo-induced electron migration
293 in TPE-AQ. Similarly, TPE-AQ also manifested a smaller radius of the semi-circular Nyquist plot
294 than TPE-FN in electrochemical impedance spectroscopy (EIS) measurements, suggesting a lower
295 charge transfer resistance in TPE-AQ. All of these results are consistent with the conclusions
296 drawn from PL analyses that less recombination and better charge carriers separation in TPE-AQ,
297 which could have a positive effect on the photocatalytic activity.

298 **Supplemental Note 2. Attribution of signals in transient absorption spectra**

299 As shown in Figures. S21 and S24, the peaks on about 650 nm could be attributed to polarons for
300 TPE-AQ. Because it decreased significantly in both electron (AgNO_3) and hole (EDTA-2Na)
301 sacrificial agents. On the other hand, peaks between 850 nm and 1300 nm could be assigned to
302 unfettered holes. Because the signal was not significantly attenuated in the presence of an electron
303 sacrificial agent but obviously decreased in the presence of a hole sacrificial agent.

304

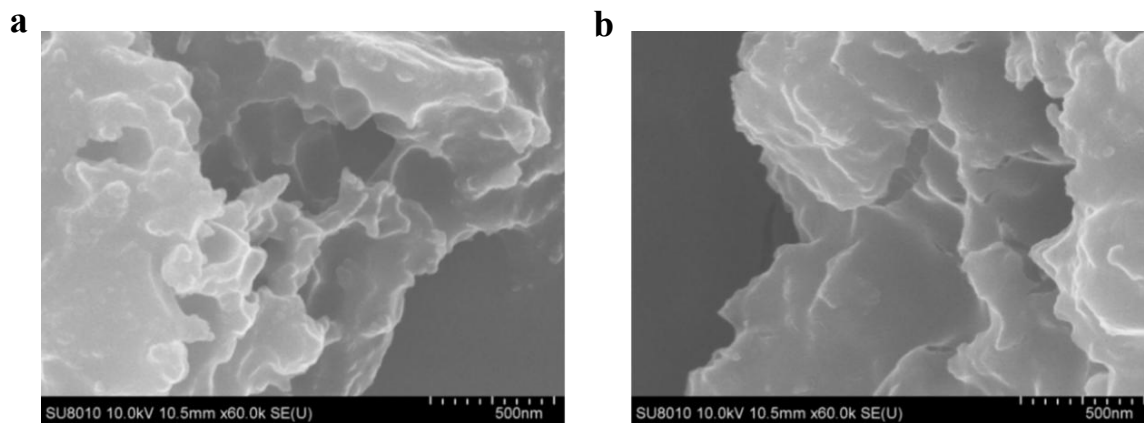


306

307 **Figure S1. PXRD patterns of TPE-AQ and TPE-FN.** The powder X-ray diffraction (PXRD)

308 profiles revealed that TPE-AQ and TPE-FN exhibited the features of amorphous carbon.

309

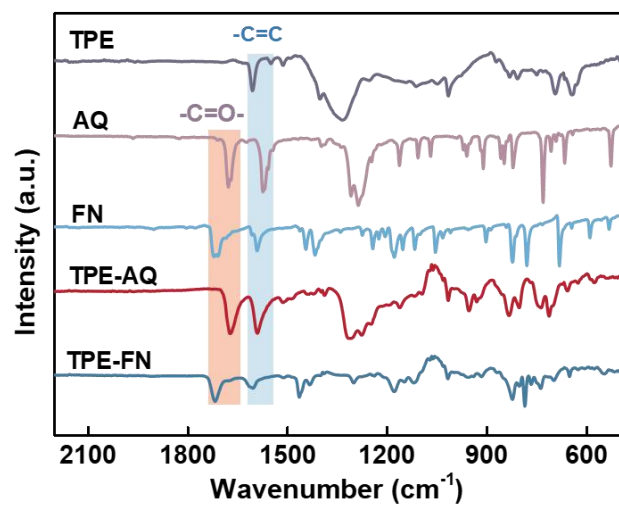


310

311 **Figure S2. Scanning electron microscope (SEM) images of CPs.** SEM images of (a) TPE-AQ

312 and (b) TPE-FN. The SEM images indicated the CPs were stratified structures.

313



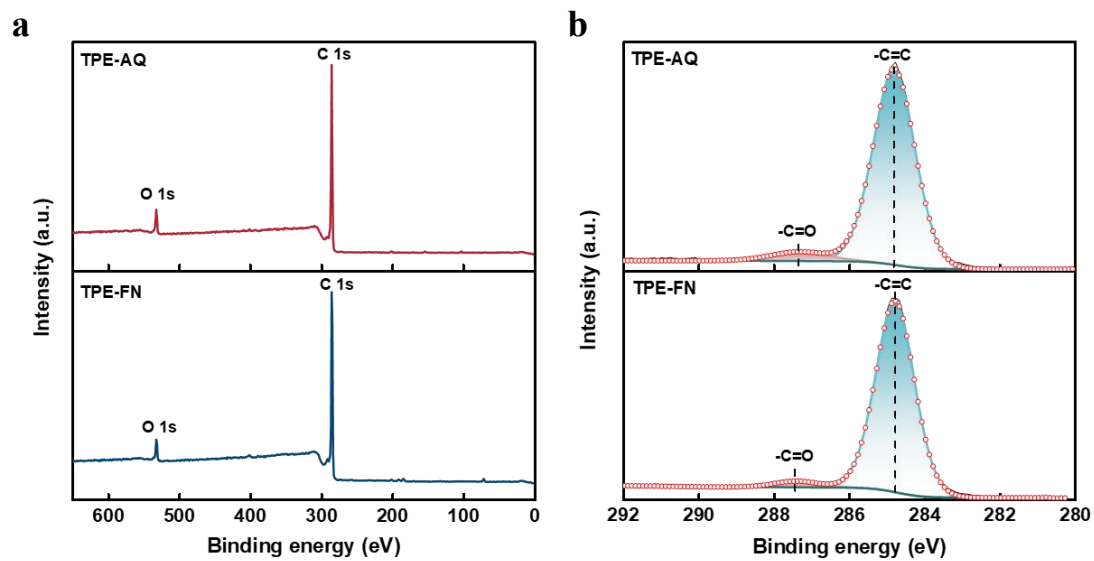
314

315 **Figure S3. FT-IR spectra of TPE-AQ, TPE-FN, and monomer.** The peaks at 1671 cm⁻¹ and

316 1716 cm⁻¹ were attributed to the carbonyl group in TPE-AQ and TPE-FN, respectively. The signal

317 at 1590 cm⁻¹ corresponded to the stretching vibration of C=C bonds in the aromatic skeletons.

318

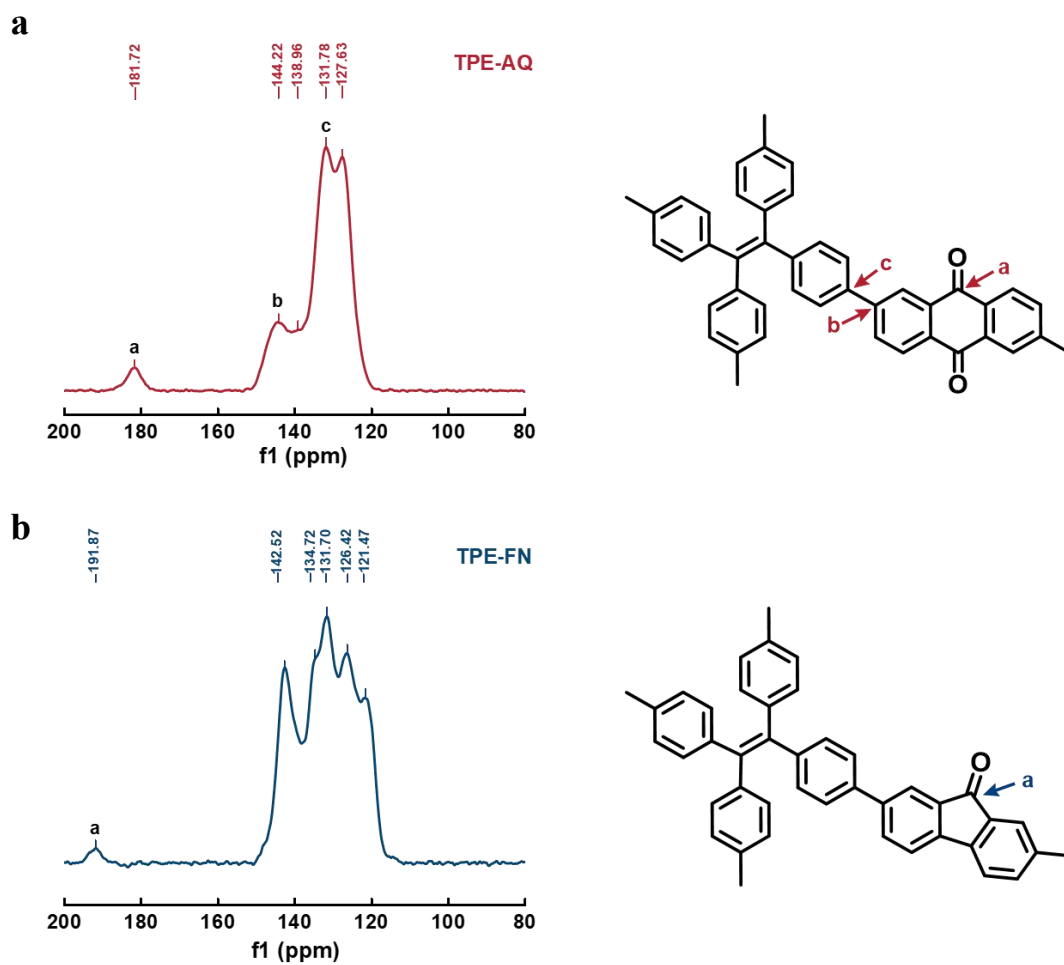


319

320 **Figure S4. The XPS spectra of TPE-AQ and TPE-FN. (a) The survey XPS spectra. (b) The**

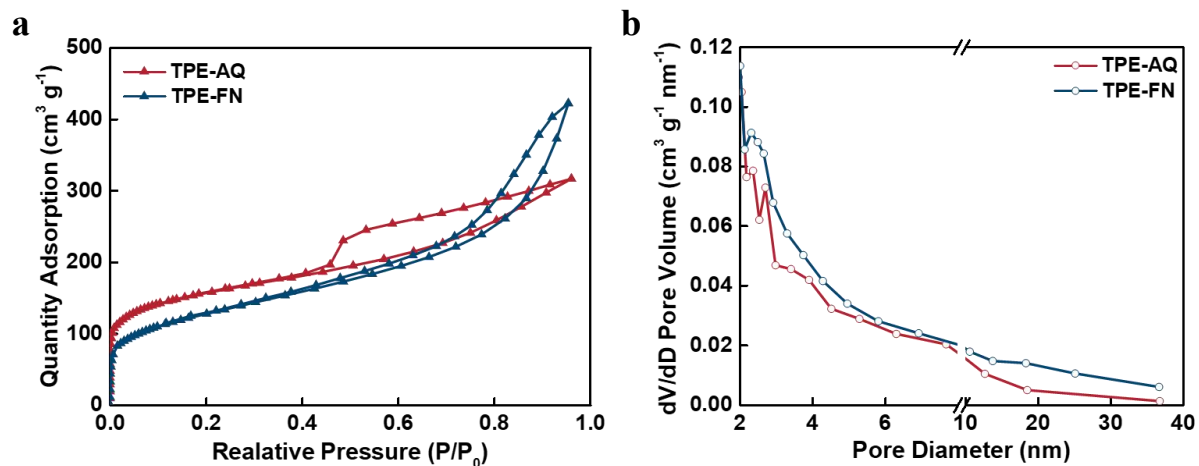
321 high-resolution C 1s XPS spectra.

322



323 **Figure S5. Solid state ^{13}C CP-MAS NMR spectra. Spectra of (a) TPE-AQ, (b) TPE-FN.**

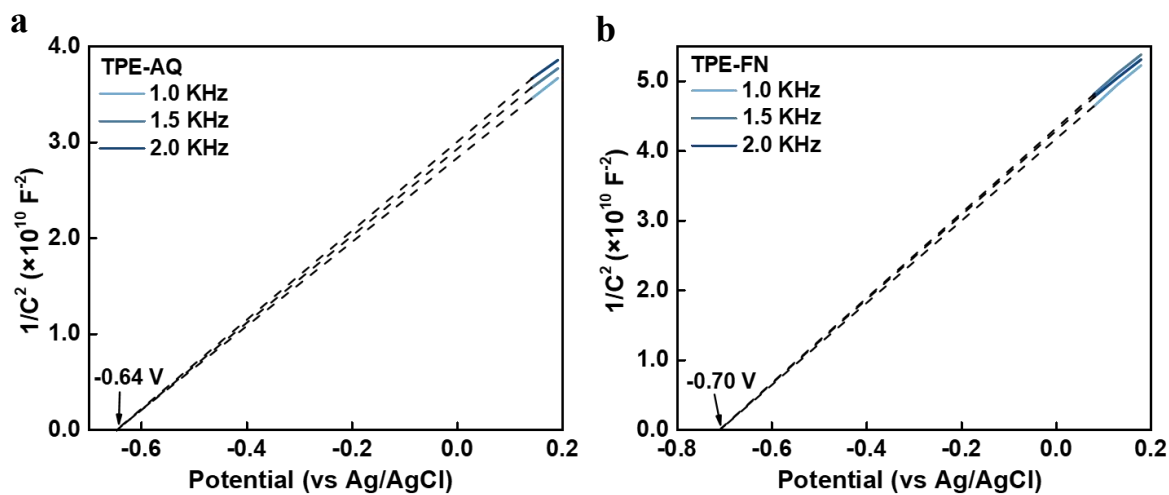
324



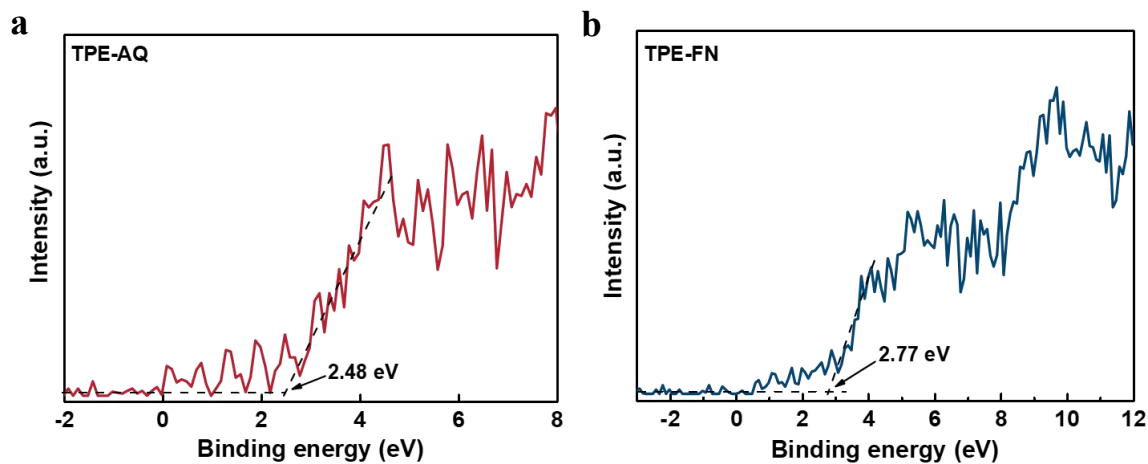
325

	TPE-AQ	TPE-FN
BET Surface ($\text{m}^2 \text{g}^{-1}$)	564.124	457.804
Pore Diameter (nm)	2.0501	2.0080

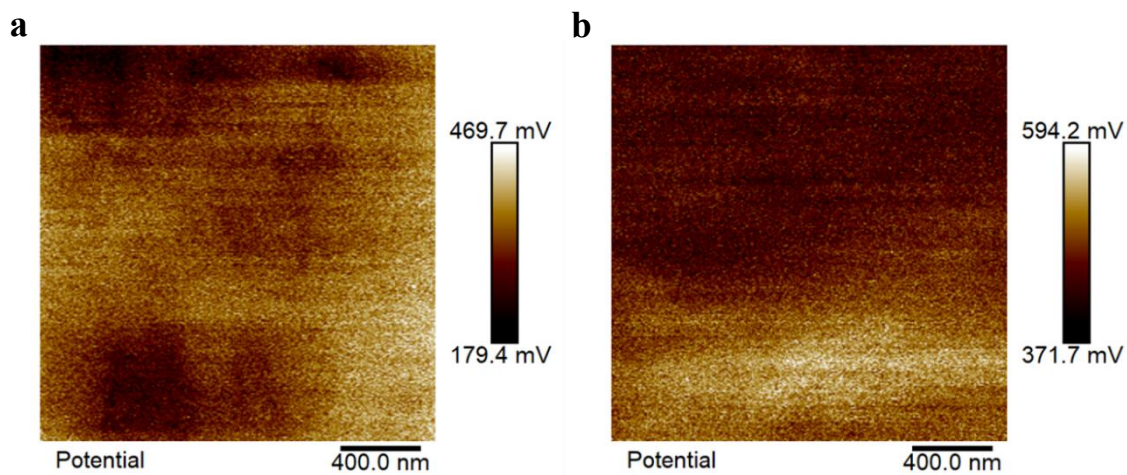
326 **Figure S6. Measurements of Brunauer-Emmett-Teller surface areas.** (a) N_2
 327 adsorption-desorption isotherms; (b) The corresponding pore size distributions of TPE-AQ and
 328 TPE-FN.
 329



330 **Figure S7. Characterization of CBM through Mott Schottky.** Mott Schottky plots of (a)
 331 TPE-AQ and (b) TPE-FN. The FTO glasses deposited with materials were used as photoelectrode.
 332 The three electrodes were inserted in a quartz cell filled with 0.5 M Na₂SO₄. The flat-band values
 333 were evaluated as -0.64 and -0.70 eV versus the Ag/AgCl electrode.
 334



335 **Figure S8. XPS valence band spectrum of CPs.** The spectrum of (a) TPE-AQ and (b) TPE-FN.
336 The valence band maximum (VBM) of TPE-AQ and TPE-FN were determined to be 2.48 and
337 2.77 eV verse Fermi level, respectively.
338



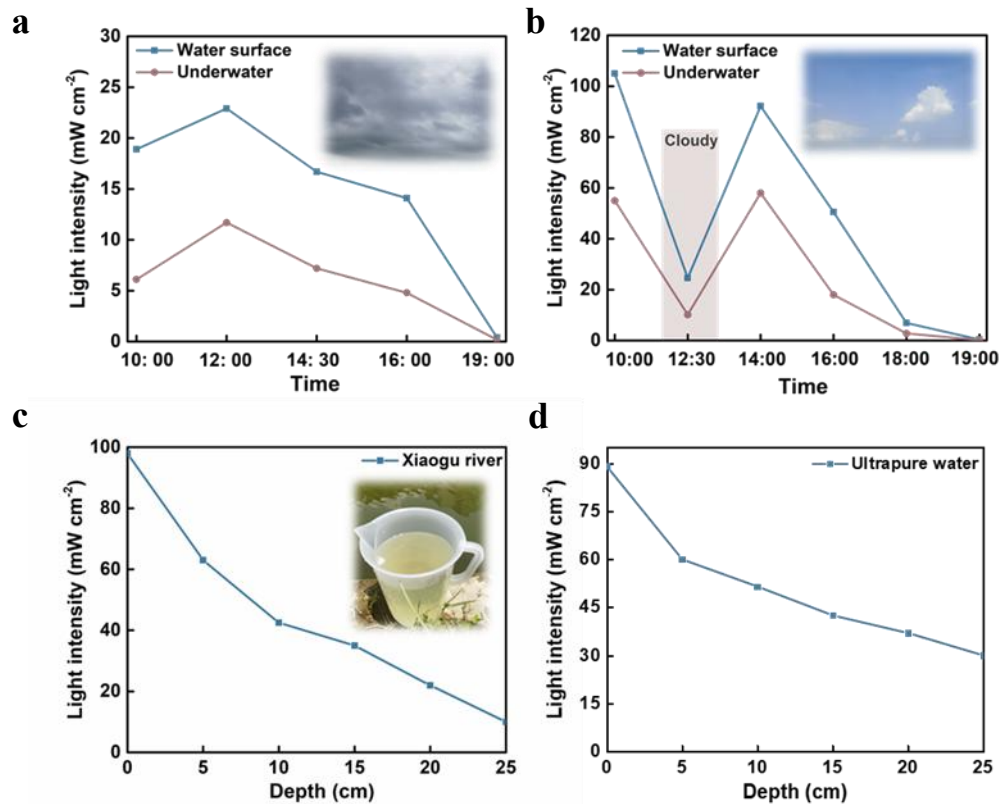
339

340 **Figure S9. Characterization of sample work function through Kelvin Probe Force**

341 **Microscopy (KPFM).** AM-KPFM images of (a) TPE-AQ and (b) TPE-FN. The work function of

342 TPE-AQ and TPE-FN were measured to be 4.233 and 4.093 eV, respectively.

343

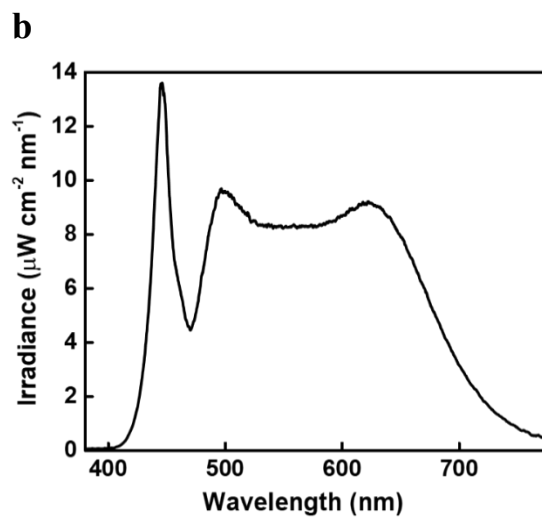
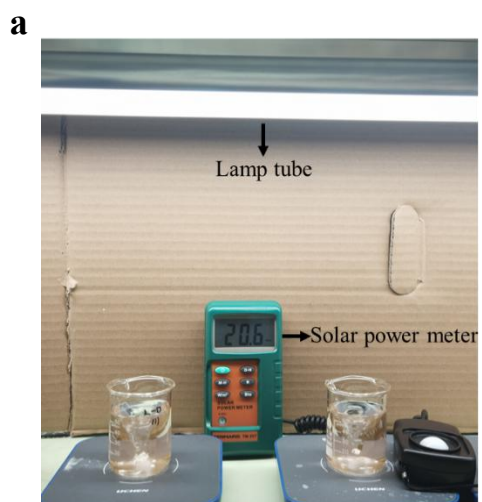


344

345 **Figure S10. Solar irradiance levels under various environmental conditions.** Variation of light
 346 intensity on the water surface and depth of 19 cm underwater on cloudy (a) and sunny days (b).

347 The attenuation of light intensity with depth in actual water (c) and ultrapure water (d).

348

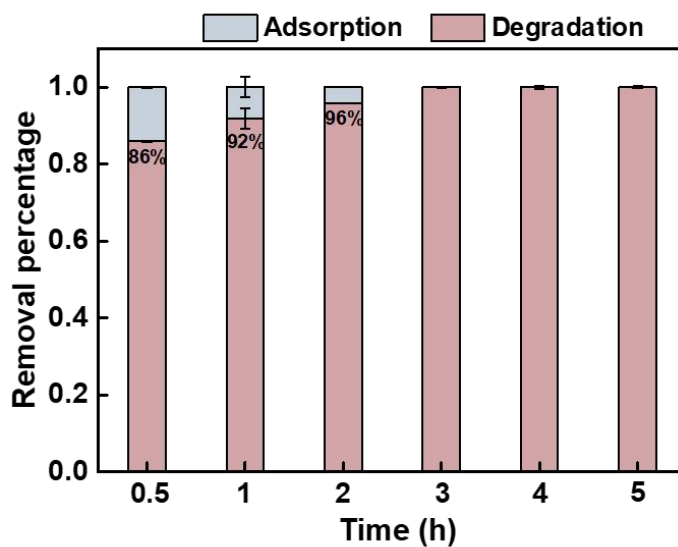


349

350 **Figure S11. The experimental device and light source spectrum.** Experimental device for

351 photocatalytic degradation of CPs **(a)** and spectrogram of lamp tube **(b)**.

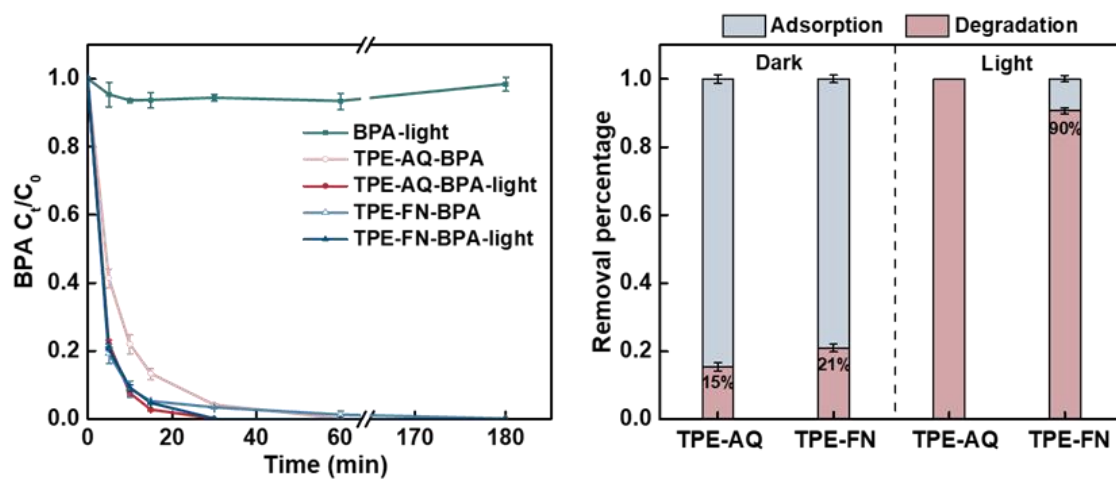
352



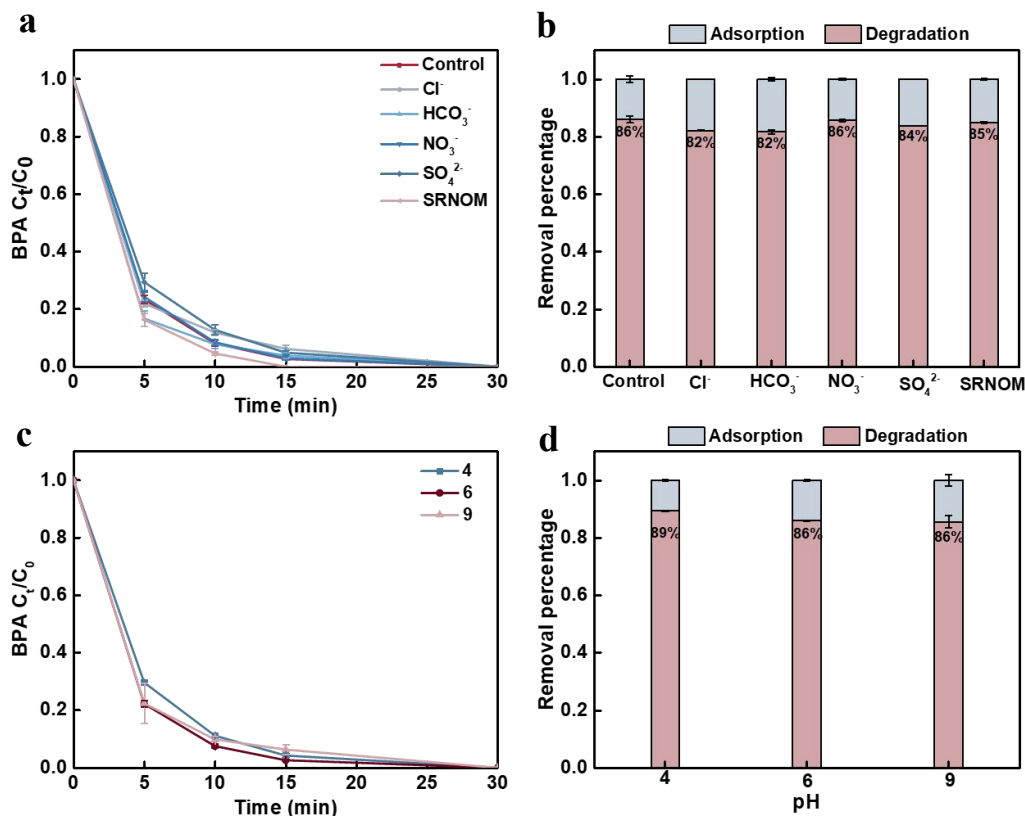
353

354 **Figure S12. Reaction condition gradient experiments.** Effects of reaction time on photocatalytic
355 degradation of BPA by TPE-AQ. Reaction conditions were: [BPA] = 2 μM , [photocatalyst] = 0.05
356 g L^{-1} , $I_0 = 2.0 \text{ mW cm}^{-2}$, [reaction time] = 1-5 h.

357



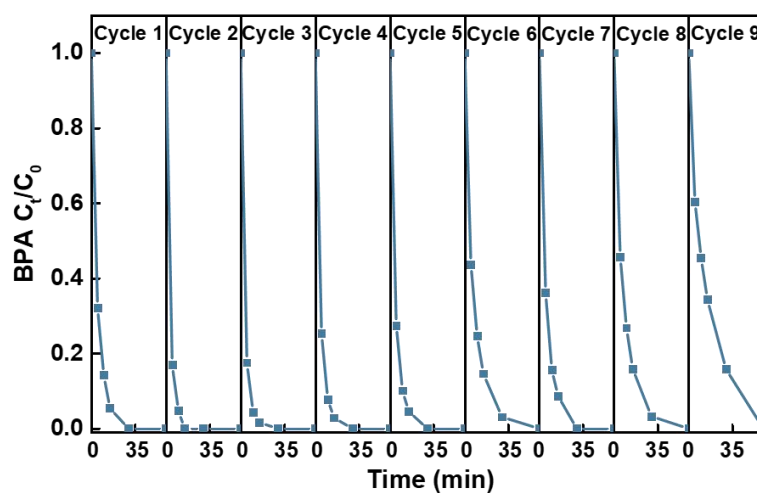
358 **Figure S13. The photocatalytic performance of CPs for BPA degradation.** Reaction conditions
 359 were: [BPA] = 2 μM , [photocatalyst] = 0.05 g L^{-1} , [reaction time] = 3 h, $I_0 = 2.0 \text{ mW cm}^{-2}$.
 360



361

362 **Figure S14. The withstand interference ability test.** Effect of (a-b) water matrix components
 363 (coexisting anions and SRNOM) and (c-d) pH on the photocatalytic performance of TPE-AQ.
 364 Reaction conditions were: (a-b) [BPA] = 2 μM, [photocatalyst] = 0.05 g L⁻¹, [anions] = 5 mM,
 365 [SRNOM] = 5 mg_C L⁻¹, [reaction time] = 30 min, I₀ = 2.0 mW cm⁻². (c-d) The condition was the
 366 same as (a-b), except the pH was adjusted to 4-9 by NaOH and H₂SO₄. TPE-AQ demonstrated
 367 exceptional resistance to interference.

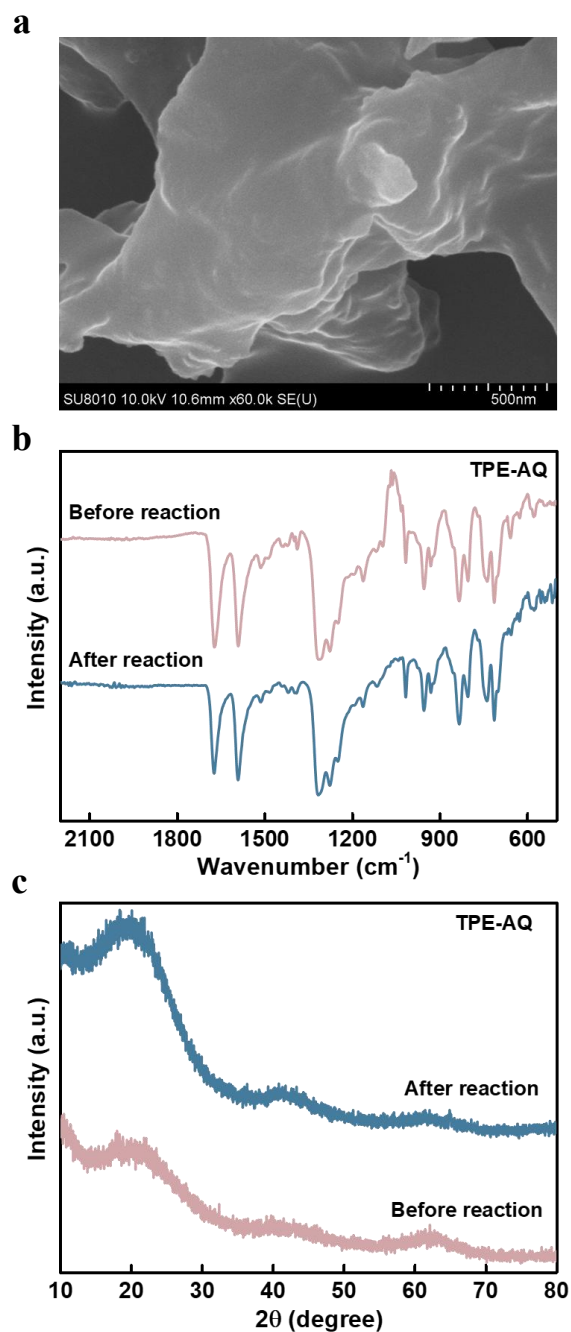
368



369

370 **Figure S15. Recycle experiments of TPE-AQ.** Reaction conditions were: [BPA] = 2 μM ,
 371 [TPE-AQ] = 0.05 g L^{-1} , [reaction time] = 3 h, $I_0 = 2.0 \text{ mW cm}^{-2}$. TPE-AQ exhibited remarkable
 372 stability over nine cycles.

373



374

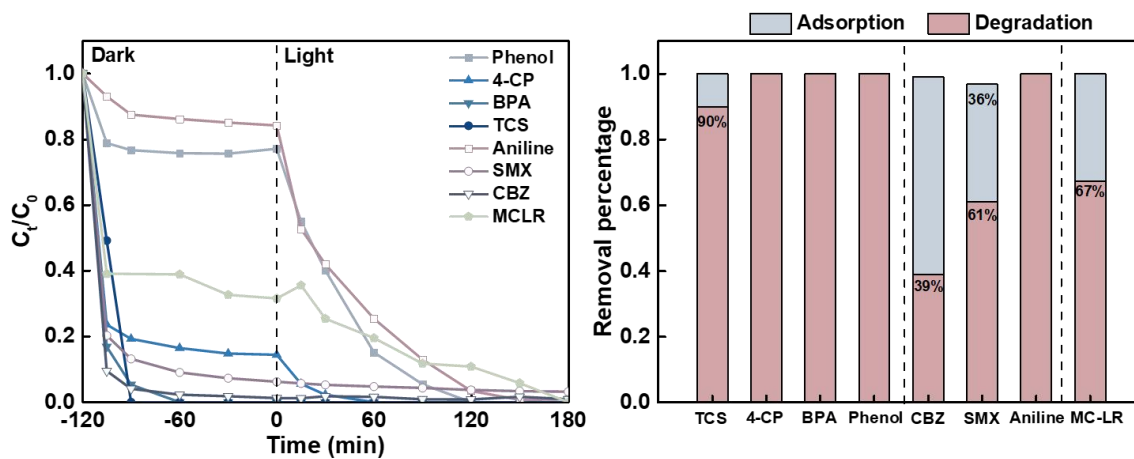
375 **Figure S16. Post-characterization of TPE-AQ after photocatalysis.** Comparison of TPE-AQ

376 before and after photoreaction: **(a)** SEM image, **(b)** FT-IR spectra, **(c)** PXRD. The composition

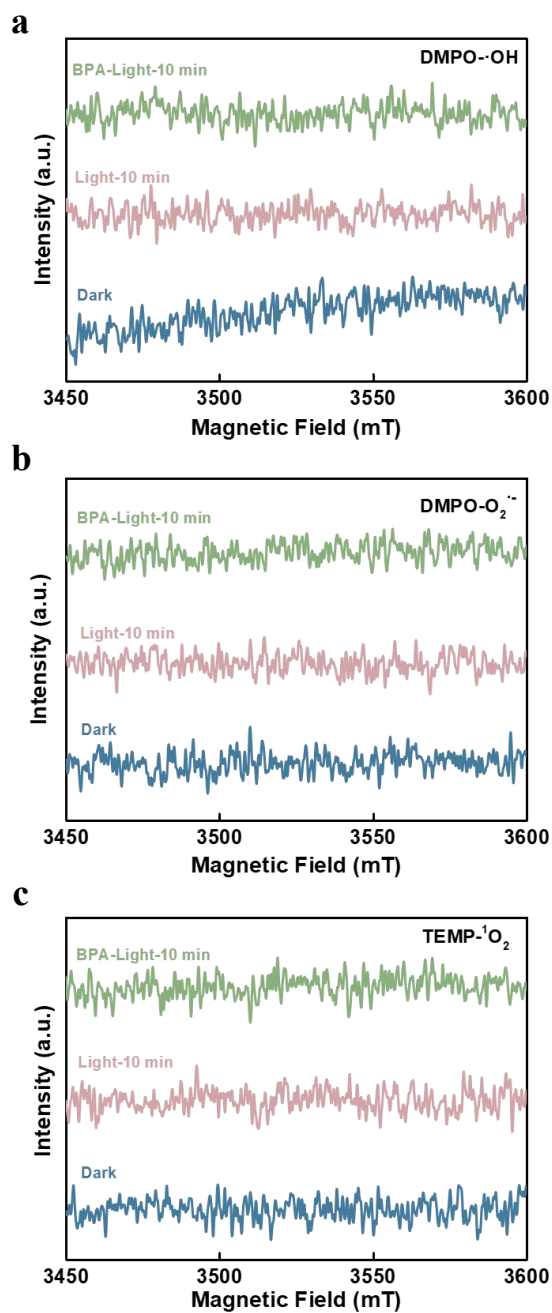
377 and structure of TPE-AQ remained unchanged after photocatalysis, this further demonstrated the

378 excellent cyclic stability of TPE-AQ.

379



380 **Figure S17. Degradation of different micropollutants in the TPE-AQ system.** Reaction
 381 conditions were: [pollutants] = 2 μM , [TPE-AQ] = 0.05 g L^{-1} , [reaction time] = 3 h, $I_0 = 2.0 \text{ mW}$
 382 cm^{-2} . TPE-AQ showcased remarkable efficacy in degrading a wide range of organic pollutants.
 383



384

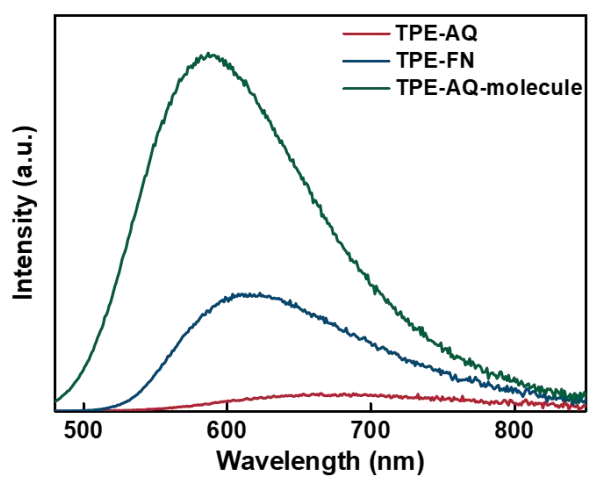
385 **Figure S18. EPR spectra of TPE-AQ.** EPR spectra of TPE-AQ in the presence of (a-b) DMPO

386 and (c) TEMP in the O₂ atmosphere. The results showed that superoxide radicals, singlet oxygen,

387 and hydroxyl radicals did not participate in the photocatalytic degradation of BPA, which was

388 consistent with the results of quenching experiment.

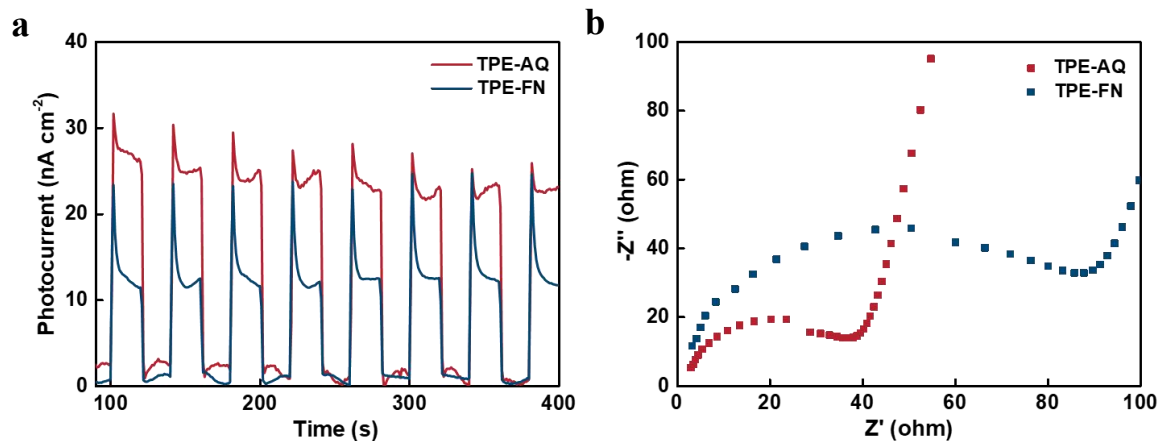
389



390

391 **Figure S19. Photoluminescence spectra of TPE-AQ, TPE-FN, and TPE-AQ-molecule.** The PL
392 intensity was negligible in TPE-AQ compared to TPE-FN and TPE-AQ-molecule, indicating the
393 better separation of photo-induced carriers in TPE-AQ.

394



395 **Figure S20. Photocurrent responses and electrochemical impedance spectroscopy analysis.**

396 Photocurrent responses **(a)** and Electrochemical impedance spectra **(b)** of TPE-AQ and TPE-FN.

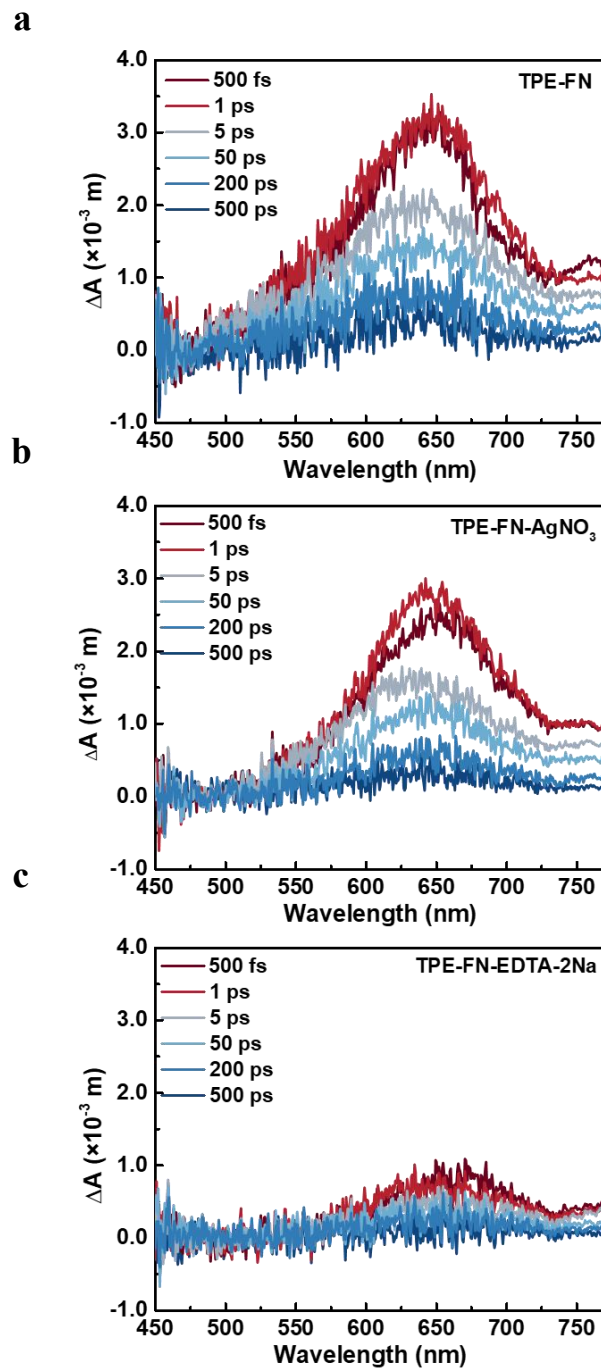
397 The Photocurrent responses measurements were performed on an FTO electrode in 0.1 M Na₂SO₄

398 solution and N₂ atmosphere and the EIS measurements were performed on a Glassy carbon

399 electrode in 0.5 M Na₂SO₄ solution. The photocurrent responses and EIS all confirmed the better

400 separation of photo-induced carriers for TPE-AQ than TPE-FN.

401



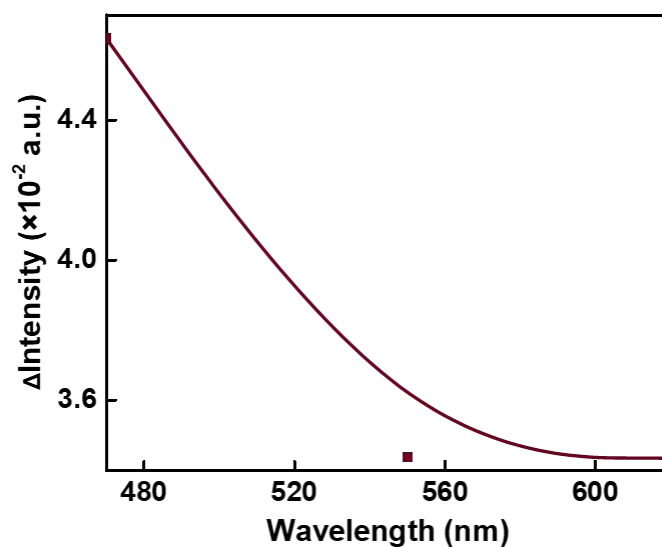
402

403 **Figure S21. Femtosecond transient absorption measurements probed at visible region.** The

404 transient absorption spectra of TPE-FN with different quenchers. TA details of CPs pumped at 400

405 nm. AgNO₃ and EDTA-2Na were all 10 mM.

406



407

408

409 **Figure S22. Δ EPR signal intensity as a function of excitation wavelength.** The EPR signal

410 was recorded at room temperature without additional light source as control, then the EPR signal

411 was measured after irradiating the material solution for 60 s at different excitation wavelengths.

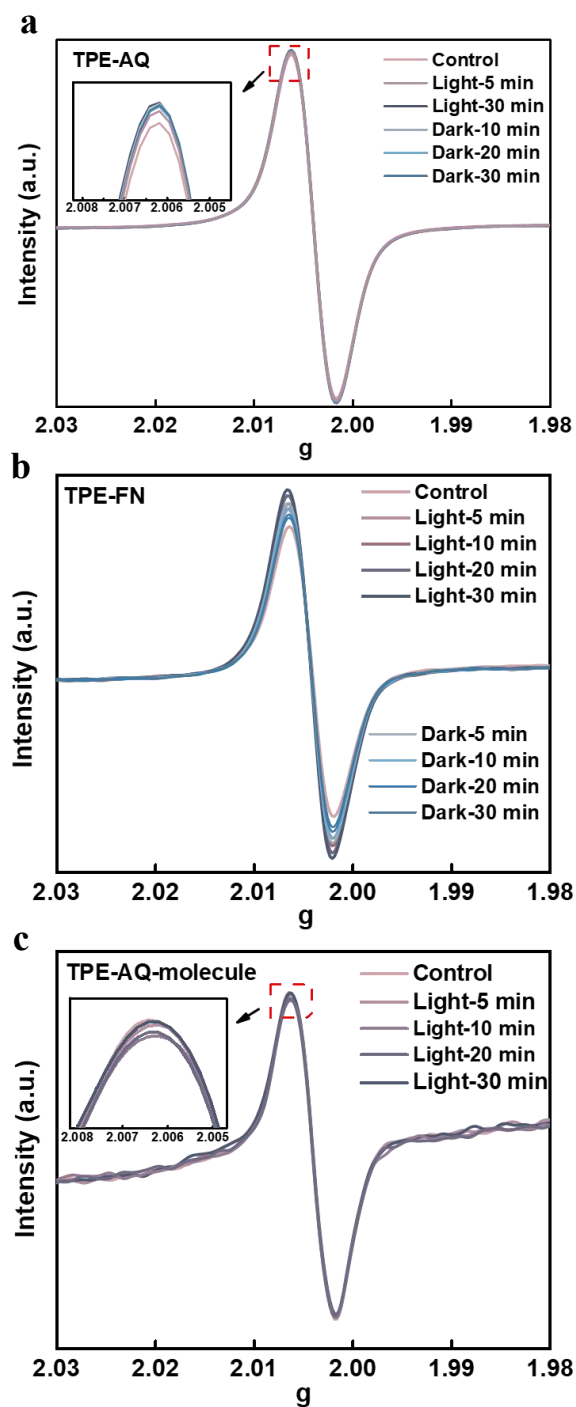
412 The relationship between EPR signal (represented by the highest point of EPR signal strength,

413 $g=2.0063$) increase and excitation wavelength was compared. In the variation of EPR signal

414 intensity with different excitation wavelengths was consistent with TPE-AQ's optical absorption

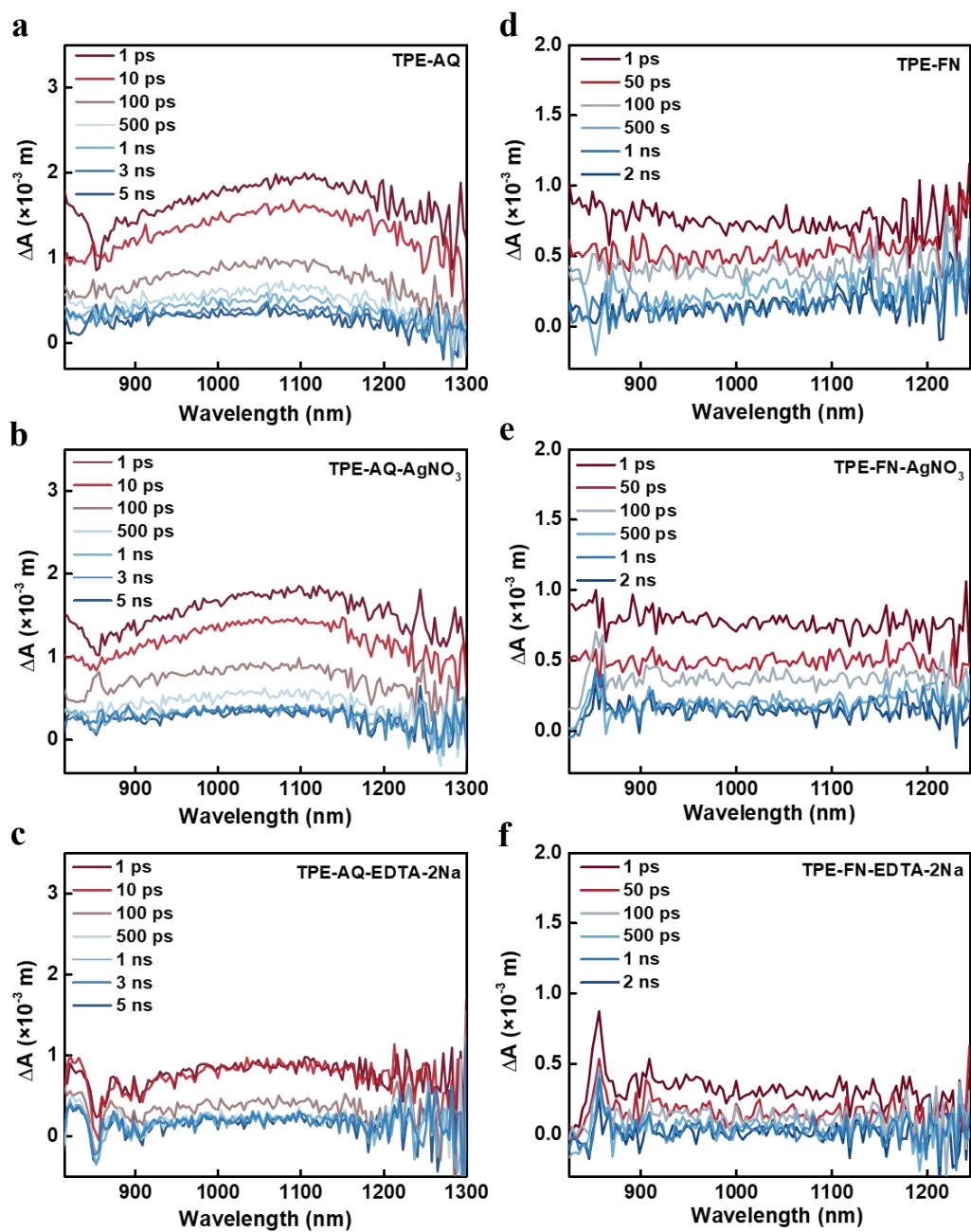
415 spectrum.

416



417

418 **Figure S23. The lifetime of OCORs.** The time-dependent in-situ solid EPR spectra of (a)
 419 TPE-AQ, (b) TPE-FN, and (c) TPE-AQ-molecule. The light was turned off after the photocatalyst
 420 (solid) was illuminated for 30 minutes. The lighting and dark processes were continually
 421 monitored.



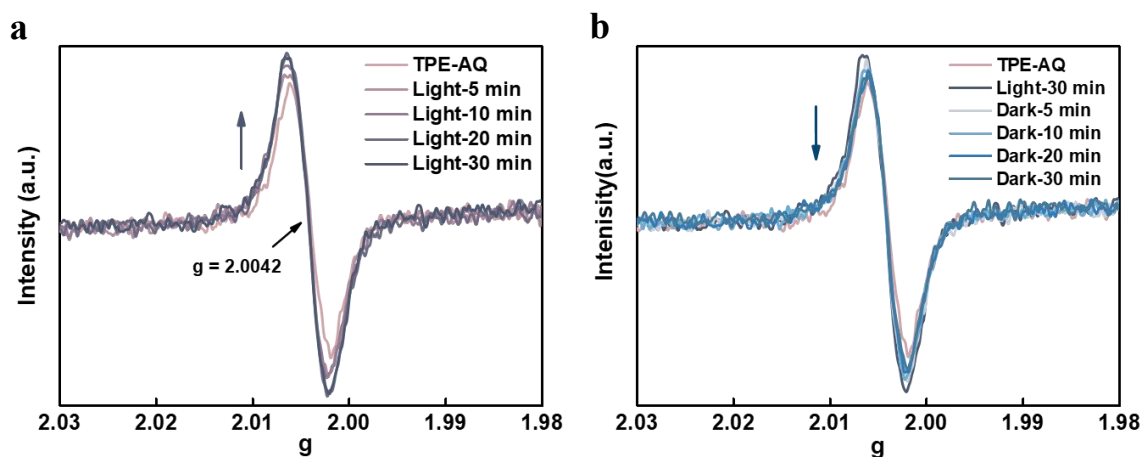
422

423 **Figure S24. Femtosecond transient absorption measurements probed at near-infrared region.**

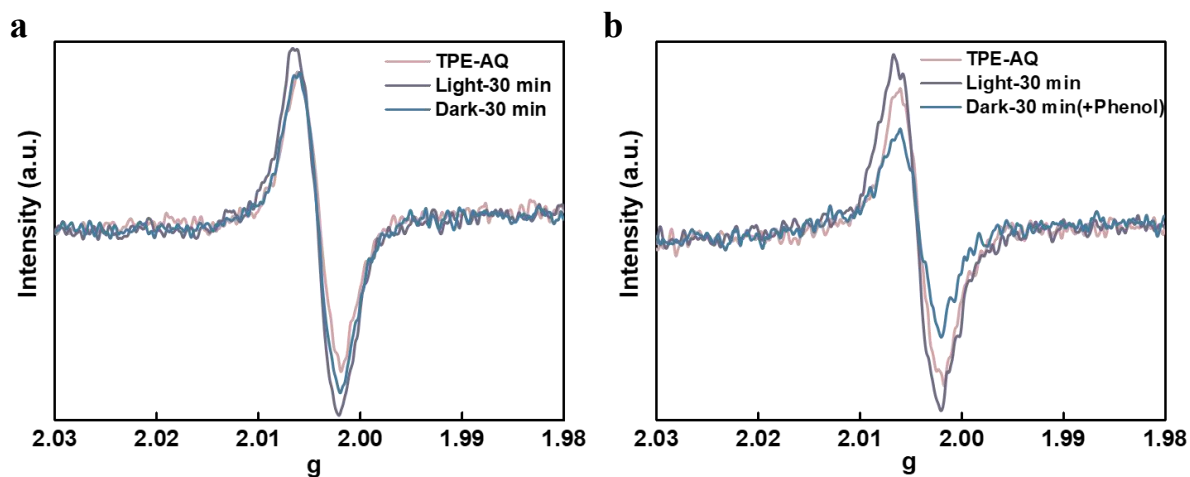
424 The transient absorption spectra of TPE-AQ (a-c) and TPE-FN (d-f) with different quenchers. TA

425 details of CPs pumped at 400 nm. AgNO₃ and EDTA-2Na were all 10 mM.

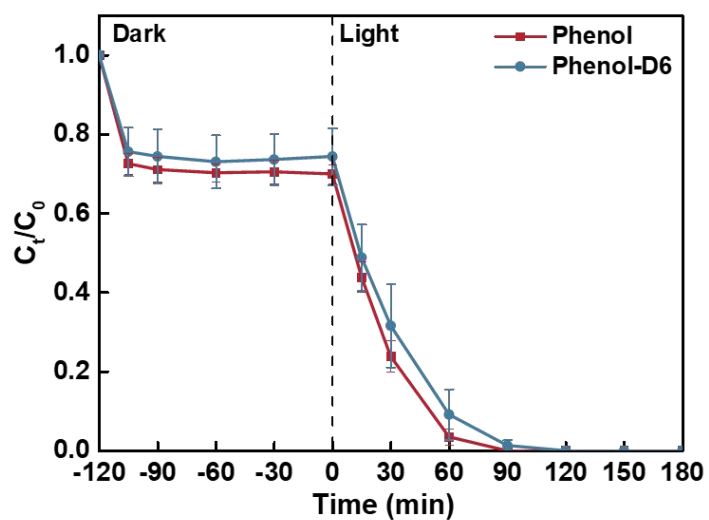
426



427 **Figure S25. The time-dependent in-situ EPR spectra of TPE-AQ in H₂O.** After 30 minutes of
 428 illumination of TPE-AQ, the light was turned off, and the lighting (a) and dark (b) processes were
 429 continuously tracked. The EPR signal intensity decreased with time after the lamp was removed,
 430 indicating the potential reactivity of OCORs with water.
 431



432 **Figure S26. Characterization of the electron storage properties of TPE-AQ.** EPR spectra of
 433 light and dark processes of TPE-AQ-H₂O in the absence **(a)** and presence **(b)** of phenol. Phenol
 434 was added after turning off the light and reacted in dark conditions. After the light source was
 435 removed, the presence of phenol accelerated the decay of the EPR signal with time, demonstrating
 436 that the light-generated OCORs could be stored and reacted with phenol in a light-independent
 437 process. The results showed that TPE-AQ had an electron storage ability.
 438

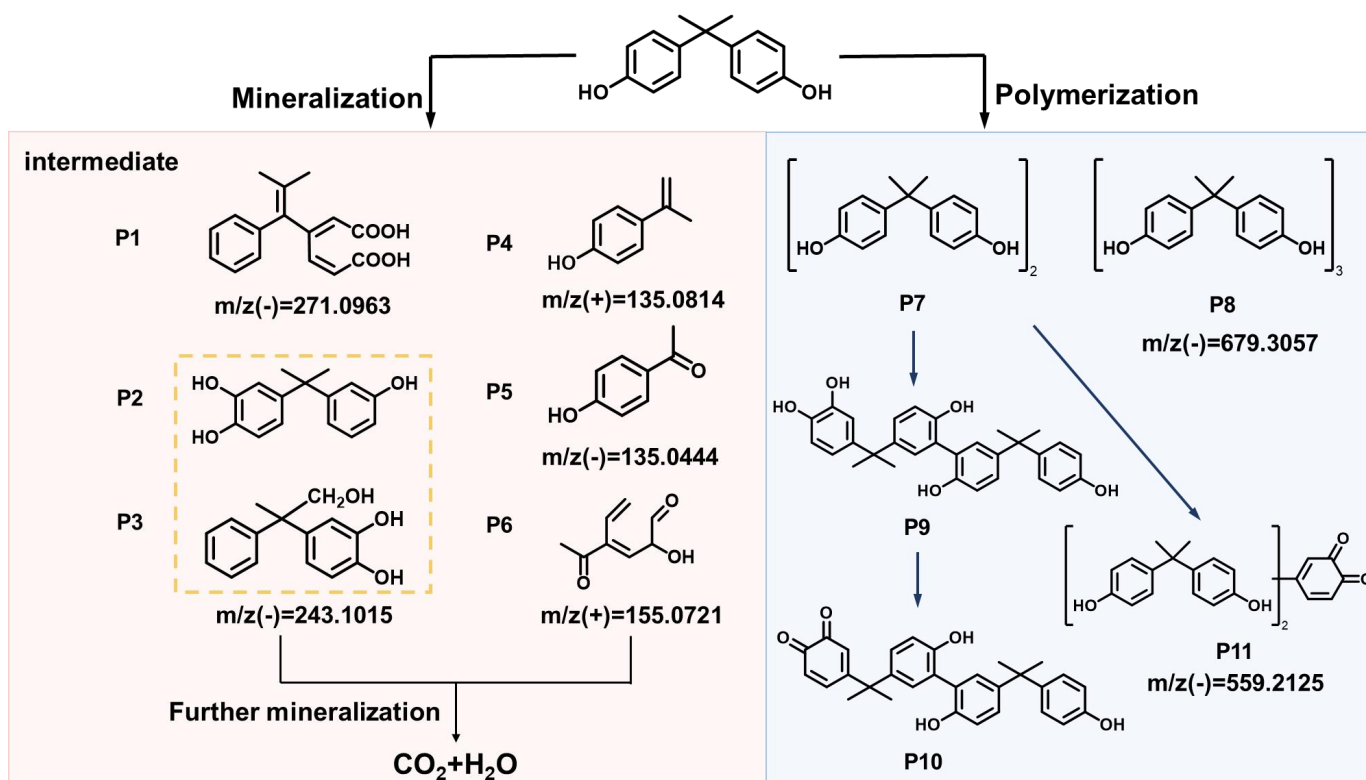


439

440 **Figure S27. H/D kinetic isotope effect for phenol degradation in TPE-AQ system.** The
 441 temporal concentration changes of phenol as a function of reaction time. Reaction conditions were:

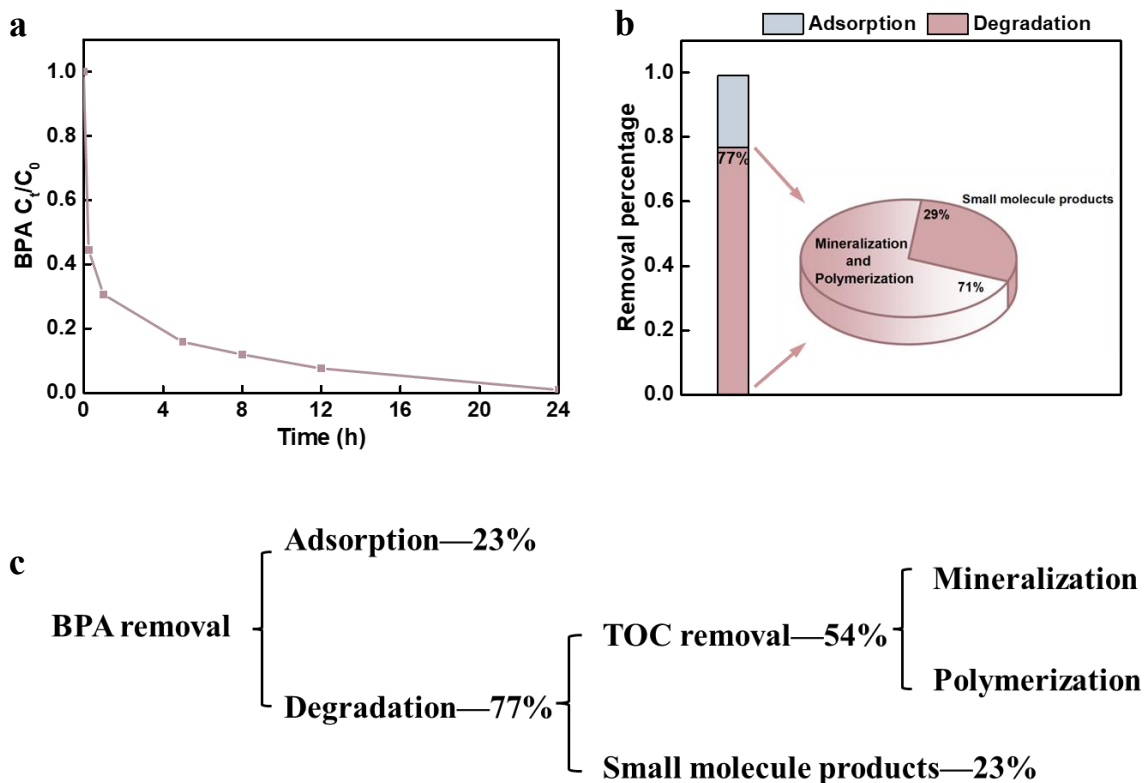
442 $[\text{phenol}] = [\text{phenol-D6}] = 2 \mu\text{M}$, $[\text{TPE-AQ}] = 0.05 \text{ g L}^{-1}$, $I_0 = 2.0 \text{ mW cm}^{-2}$.

443

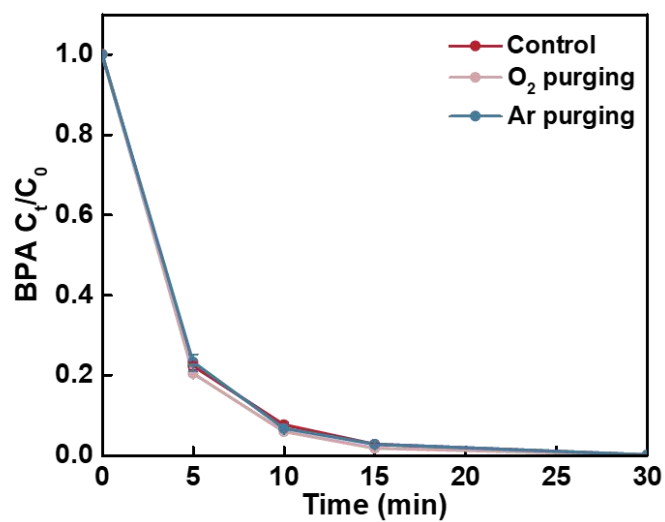


444 Figure S28. Photocatalytic degradation pathway of BPA.

445



446 **Figure S29. TOC removal in the TPE-AQ system.** The temporal concentration changes of BPA
 447 as a function of reaction time **(a)** and BPA removal pathway and proportion of each pathway **(b-c)**.
 448 Reaction conditions were: [BPA] = 100 μM , [TPE-AQ] = 0.1 g L^{-1} , [reaction time] = 24 h, $I_0 = 2.0$
 449 mW cm^{-2} .
 450



451

452 **Figure S30. Effect of atmospheric on the photocatalytic performance of TPE-AQ.**

453 Photocatalytic degradation of BPA by TPE-AQ with purging O₂ or Ar. Reaction conditions were:

454 [BPA] = 2 μM, [TPE-AQ] = 0.05 g L⁻¹, [reaction time] = 30 min, I₀ = 2.0 mW cm⁻². In the absence

455 of oxygen, the degradation of BPA was inhibited by 37%.

456

458 **Table S1. Photocatalytic activity and light intensity between TPE-AQ and other reported**
459 **photocatalysts for micropollutants degradation.**

Catalyst	Condition	Adsorption time	Reaction time (min)	Light intensity (mW cm ⁻²)	Degradation rate/%	Ref
Fc-TEB-CMP	0.25 g L ⁻¹ Cat, 0.10 mM (MB)	60 min	120	100 ($\lambda > 400$ nm)	99	2
Cs ₂ AgBiBr ₆	2.0 g L ⁻¹ Cat, 0.20 mM (RhB)	60 min	120	110 ($\lambda > 420$ nm) 33 ($\lambda > 420$ nm)	100 20	3
LZS	0.2 g L ⁻¹ Cat, 0.15 mM (4-CP)	30 min	10	326 (320 < λ < 780 nm)	100	4
TiO ₂ -10	0.2 g L ⁻¹ Cat, 0.40 mM (Phenol)	20 min	80	100 (300 W xenon lamp)	60	5
AMM	20 g L ⁻¹ Cat, 0.02 mM (tetracycline)	30 min	120	85 ($\lambda > 400$ nm)	92.6	6
2DZnTcpp	0.2 g L ⁻¹ Cat, 0.03 mM (MB)	12 h	/	/	31	7
	0.2 g L ⁻¹ Cat, 0.03 mM (MB)	/	60	100 (xenon lamp)	46.2	
WUCN-500	0.2 g L ⁻¹ Cat, 0.28 mM (OA)	30 min	30	350 (320 < λ < 800 nm)	43	8
ACN0.5	0.5 g L ⁻¹ Cat, 0.01 mM (MB)	60 min	300	38 ($\lambda > 400$ nm)	100	9
10CBBR-4	0.1 g L ⁻¹ Cat, 0.047 mM (Norfloxacin)	60 min	120	50 ($\lambda > 400$ nm)	~90	10
COF-TD1	0.3 g L ⁻¹ Cat, 0.02 mM (BPA)	30 min	120	125 ($\lambda > 420$ nm)	>97%	11
G_THS	0.125 g L ⁻¹ Cat, 0.02 mM (CIP)	60 min	360	135 (AM 1.5G)	82	12
g-C ₃ N ₄	0.5 g L ⁻¹ Cat, 0.09 mM (BPA)	30 min	60	180 (300 W xenon lamp)	~35	13
TPE-AQ	0.05 g L ⁻¹ Cat, 0.002 mM (BPA)		60 min	2.0 ($\lambda > 400$ nm)	92	This work

460 **Table S2. The HPLC conditions for analysis of different micropollutants.**

micropollutant	Time (min)	Flow (mL/min)	λ (nm)	Methanol %	Acetonitrile %	Water %	0.1% Acetic acid water	0.1% Phosphoric water
Bisphenol A (BPA)	7.1	1.0	226	/	50	/	50	/
p-chlorophenol (4-CP)	5.6	1.0	220	/	55	/	45	/
Phenol	8	1.0	270	55	/	/	45	/
Triclosan (TCS)	15.5	1.0	281	/	70	/	30	/
Aniline	4.25	1.0	232	/	45	55	/	/
Sulfamethoxazole (SMX)	3.2	1.0	271	50	/	/	50	/
carbamazepine (CBZ)	4.0	1.0	286	/	60	/	40	/
	0				30			70
	5.5				30			70
MC-LR	6.5	1.0	238	/	90	/	/	10
	10				90			10
	10.5				30			70
	17.5				30			70

Table S3. Atomic coordinates of the TPE-AQ optimized computational model.

Atom	x	y	z
C	-4.138085	0.601535	-0.077462
C	-3.333421	-0.498083	0.000073
C	-5.625508	0.509824	-0.028682
C	-3.861124	-1.888101	-0.123041
C	-1.861881	-0.400676	0.208572
C	-3.593924	1.982223	-0.223783
C	-4.072981	3.026430	0.585675
C	-3.572731	4.321009	0.450637
C	-2.599668	4.600887	-0.512701
C	-2.133022	3.576300	-1.340698
C	-2.625890	2.280165	-1.197659
C	-3.488452	-2.876801	0.803135
C	-3.970110	-4.180444	0.687803
C	-4.816625	-4.525079	-0.369392
C	-5.176181	-3.556111	-1.310080
C	-4.702562	-2.250650	-1.188028
C	-6.412701	1.209533	-0.959172
C	-7.804580	1.136178	-0.915223
C	-8.436901	0.379650	0.075140
C	-7.665842	-0.301209	1.021204
C	-6.274322	-0.236544	0.969496
C	-1.317217	0.415927	1.214172
C	0.056300	0.484117	1.416924
C	0.943222	-0.260093	0.618689
C	0.398261	-1.087273	-0.379241
C	-0.976856	-1.165407	-0.570324
C	2.407213	-0.179505	0.825503
C	2.954184	-0.024271	2.115486
C	4.327686	0.057724	2.306278
C	5.203658	-0.015522	1.217033
C	4.672673	-0.173188	-0.079064
C	3.291579	-0.251406	-0.261433
C	6.668751	0.073247	1.448227
C	7.559990	-0.002870	0.255818

C	7.032009	-0.156101	-1.042871
C	5.563083	-0.246210	-1.273019
O	5.101530	-0.376331	-2.405173
O	7.130470	0.205342	2.581207
H	-4.835105	2.813699	1.329242
H	-3.944160	5.112095	1.095482
H	-2.214164	5.610134	-0.622420
H	-1.387846	3.787698	-2.102057
H	-2.262283	1.485501	-1.840783
H	-2.823913	-2.613891	1.620712
H	-3.682714	-4.927879	1.421525
H	-5.187206	-5.541498	-0.463192
H	-5.822542	-3.818388	-2.142608
H	-4.984189	-1.498505	-1.917707
H	-5.924674	1.805884	-1.724171
H	-8.395784	1.671976	-1.652128
H	-9.520876	0.327411	0.113905
H	-8.148793	-0.879625	1.803423
H	-5.677423	-0.766841	1.704094
H	-1.982373	1.008908	1.832541
H	0.445712	1.140696	2.188651
H	1.054787	-1.696683	-0.992308
H	-1.375878	-1.825202	-1.334247
H	2.294863	0.009289	2.976492
H	4.744217	0.170089	3.301096
H	2.916615	-0.347244	-1.274058
C	8.945388	0.079289	0.434412
C	9.800492	0.010156	-0.663263
C	9.276516	-0.142359	-1.952071
C	7.898664	-0.224899	-2.139674
H	9.332344	0.196954	1.440426
H	10.874080	0.074462	-0.517647
H	9.943219	-0.196481	-2.806743
H	7.473592	-0.342989	-3.130186

Table S4. Atomic coordinates of the TPE-FN optimized computational model.

Atom	x	y	z
C	-3.794548	-0.552838	0.027218
C	-2.917011	0.492687	0.031637
C	-5.258123	-0.370724	-0.192107
C	-3.359823	1.915855	0.084490
C	-1.441381	0.292828	-0.011876
C	-3.358589	-1.962441	0.245611
C	-3.808091	-2.988047	-0.603494
C	-3.410595	-4.309104	-0.399887
C	-2.573899	-4.633640	0.671449
C	-2.139894	-3.626554	1.537794
C	-2.528844	-2.304664	1.326825
C	-4.307297	2.347056	1.028333
C	-4.699418	3.683496	1.086703
C	-4.151009	4.616736	0.202550
C	-3.198242	4.203797	-0.732535
C	-2.799129	2.868537	-0.783261
C	-6.188595	-1.008156	0.646353
C	-7.559078	-0.850101	0.442976
C	-8.026155	-0.068718	-0.617219
C	-7.111215	0.551734	-1.472408
C	-5.741365	0.401870	-1.261850
C	-0.848478	-0.566301	-0.952226
C	0.530344	-0.738190	-0.998115
C	1.376039	-0.058082	-0.103511
C	0.783763	0.815418	0.825836
C	-0.595113	0.995548	0.862180
C	2.845330	-0.248023	-0.143420
C	3.402699	-1.507831	-0.435360
C	4.786651	-1.721495	-0.484103
C	5.634154	-0.650817	-0.230251
C	5.085958	0.613531	0.065784
C	3.720614	0.829817	0.111692
C	7.110317	-0.542916	-0.203989
C	7.455558	0.790326	0.103554

C	6.202786	1.585280	0.286431
C	8.106171	-1.486973	-0.421527
C	9.445938	-1.076318	-0.326139
C	9.782561	0.246619	-0.021044
C	8.777486	1.199272	0.198148
O	6.108539	2.773887	0.558334
H	-4.465676	-2.740438	-1.431324
H	-3.756244	-5.085859	-1.075779
H	-2.269025	-5.663125	0.834108
H	-1.501314	-3.871395	2.381579
H	-2.189141	-1.523591	1.999096
H	-4.735467	1.624055	1.714853
H	-5.429917	3.997908	1.826456
H	-4.457877	5.657456	0.246900
H	-2.763482	4.922377	-1.421222
H	-2.052104	2.553322	-1.505621
H	-5.829406	-1.622764	1.466256
H	-8.262597	-1.339160	1.110475
H	-9.093266	0.049673	-0.780008
H	-7.464826	1.149299	-2.307618
H	-5.032593	0.886011	-1.925576
H	-1.480952	-1.097018	-1.655856
H	0.959318	-1.385663	-1.756591
H	1.406974	1.341082	1.542785
H	-1.028814	1.674849	1.589504
H	2.738433	-2.348762	-0.607672
H	5.176727	-2.709616	-0.707284
H	3.336677	1.823702	0.319459
H	7.862778	-2.517805	-0.659349
H	10.236150	-1.802067	-0.493053
H	10.826830	0.534462	0.045569
H	9.017629	2.231132	0.435780

466

467

Catalyst	D (Å)	S_m	S_r	H (Å)	t (Å)	E (eV)	HDI	EDI
TPE-AQ	8.555	0.10165	0.30385	3.393	5.852	2.466	5.38	8.20
TPE-FN	5.105	0.29071	0.53185	3.969	1.617	2.753	4.55	8.78

468 **Table S5. Time-dependent density functional theory (TD-DFT) of TPE-AQ and TPE-FN.**

469

470 **Table S6. Water quality parameters of the actual water.**

471 Water sources	pH	TOC (mgC/L)	TN (mg/L)	Dissolved oxygen (mg/L)	Cl ⁻ (mg/L)	SO ₄ ²⁻ (mg/L)	NO ₃ ⁻ (mg/L)
Beijiang River	7.49	1.72	2.04	10.82	6.36	18.29	1.81
Xiaogu River	7.60	3.30	3.52	10.40	29.50	22.13	1.34
Sea Water	8.39	2.24	0.61	9.87	19430.76	2178.94	7.52

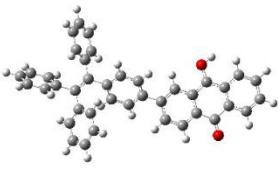
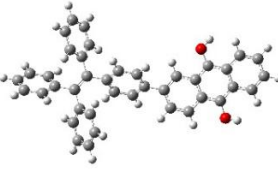
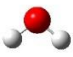



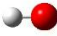
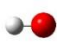
472 **Table S7. Summary of the half-life and redox potential of common transient active species**
 473 **and OCORs.**

radical	Potential (V) vs NHE	half-life	Ref
$\cdot\text{OH}$	1.80-2.70	10^{-10} s	14, 15
$\text{SO}_4^{\cdot-}$	2.50-3.10	$3.0\text{-}4.0 \times 10^{-5}$ s	14, 16
$\text{O}_2^{\cdot-}$	-0.33 ($\text{O}_2 + \text{e}^- \rightarrow \text{O}_2^{\cdot-}$) 0.91 ($\text{O}_2^{\cdot-} + \text{e}^- + 2\text{H}^+ \rightarrow \text{H}_2\text{O}_2$)	10^{-6} s	15, 17, 18
$^1\text{O}_2$	0.81 ($^1\text{O}_2 + \text{e}^- \rightarrow \text{O}_2^{\cdot-}$)	10^{-6} s (in water) 10^{-2} s (in the air)	15, 17, 19
oxygen-centered organic radicals (OCORs)	1.50 ^a	7 min	This work

474 a: represented by the half-wave potential.

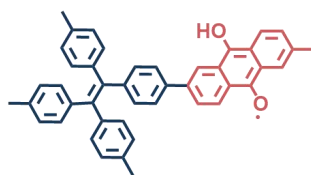
475

476 **Table S8. Single-point energy of each substance.**

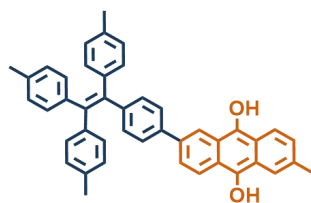
Substance	Optimized structure	Single-point energy (a.u.)
OCORs		-1689.1633
anthrahydroquinone		-1689.7609
H ₂ O		-76.3825
BPA		-730.8941
BPA ⁺⁺		-730.6780
BPA [·]		-730.2672
·OH		-75.6999
OH ⁻		-75.8819

477 The structural formula of OCORs and anthrahydroquinone in the computational
478 model:

OCORs



anthrahydroquinone



479

480

Table S9. Identification of transformation products of BPA in the TPE-AQ system.

Code	RT (min)	Formula	m/z [M-H] ⁻	m/z [M+H] ⁺	Δ (ppm)	System
P1	5.985	C ₁₆ H ₁₆ O ₄	271.0963	/	-2.6	Reaction (water)
P2	5.240	C ₁₅ H ₁₆ O ₃	243.1015	/	-2.5	Desorption (acetonitrile)
P3						
P4	3.237	C ₉ H ₁₀ O	/	135.0814	3.0	Reaction (water)
P5	3.466	C ₈ H ₈ O ₂	135.0444	/	-1.5	Reaction (water)
P6	4.324	C ₈ H ₁₀ O ₃	/	155.0721	8.4	Desorption (acetonitrile)
	6.915		453.2071	/	1.1	
P7	7.070	C ₃₀ H ₃₀ O ₄	453.2084	/	4.0	
	7.646		453.2079	/	2.9	
P8	8.046	C ₄₅ H ₄₄ O ₆	679.3067	/	1.0	
	6.671		469.2016	/	0.2	Desorption (acetonitrile)
P9	6.878	C ₃₀ H ₃₀ O ₅	469.2026	/	2.3	
	6.929		469.2028	/	2.8	
	7.080		469.2031	/	3.4	
P10	7.267	C ₃₀ H ₂₈ O ₅	467.1861	/	0.6	
	8.015		467.1857	/	-0.2	
P11	8.357	C ₃₆ H ₃₂ O ₆	559.2125	/	0.7	

Table S10. Baseline toxicity data predicted using the ECOSAR program of EPI Suite 4.0.

Code	Formula	Organism	Duration (h)	End Pt	Concentration (mg L ⁻¹)
BPA	C ₁₅ H ₁₆ O ₂	Fish	96	LC50	6.274
		Daphnid	48	LC50	4.146
		Green Algae	96	EC50	5.782
P1	C ₁₆ H ₁₆ O ₄	Fish	96	LC50	117.768
		Daphnid	48	LC50	76.264
		Green Algae	96	EC50	97.829
P2	C ₁₅ H ₁₆ O ₃	Fish	96	LC50	18.122
		Daphnid	48	LC50	11.456
		Green Algae	96	EC50	13.302
P3	C ₁₅ H ₁₆ O ₃	Fish	96	LC50	138.825
		Daphnid	48	LC50	80.134
		Green Algae	96	EC50	63.894
P4	C ₉ H ₁₀ O	Fish	96	LC50	15.074
		Daphnid	48	LC50	9.354
		Green Algae	96	EC50	10.061
P5	C ₈ H ₈ O ₂	Fish	96	LC50	592.967
		Daphnid	48	LC50	312.526
		Green Algae	96	EC50	171.100
P6	C ₈ H ₁₀ O ₃	Fish	96	LC50	4.26×10 ⁴
		Daphnid	48	LC50	1.87×10 ⁴
		Green Algae	96	EC50	4749.775
P7	C ₃₀ H ₃₀ O ₄	Fish	96	LC50	0.011
		Daphnid	48	LC50	0.010
		Green Algae	96	EC50	0.050
P8	C ₄₅ H ₄₄ O ₆	Fish	96	LC50	1.38×10 ⁻⁵
		Daphnid	48	LC50	1.71×10 ⁻⁵
		Green Algae	96	EC50	3.24×10 ⁻⁴
P9	C ₃₀ H ₃₀ O ₅	Fish	96	LC50	0.030
		Daphnid	48	LC50	0.026
		Green Algae	96	EC50	0.111

		Fish	96	LC50	0.022
P10	C ₃₀ H ₂₈ O ₅	Daphnid	48	LC50	0.019
		Green Algae	96	EC50	0.088
		Fish	96	LC50	0.005
P11	C ₃₆ H ₃₂ O ₆	Daphnid	48	LC50	0.005
		Green Algae	96	EC50	0.031

484

485

486 **Supplemental References**

- 487 1. Z. Lan, M. Wu, Z. Fang, X. Chi, X. Chen, Y. Zhang and X. Wang, A fully coplanar
488 donor–acceptor polymeric semiconductor with promoted charge separation kinetics for
489 photochemistry, *Angew. Chem. Int. Ed.*, 2021, **60**, 16355-16359.
- 490 2. L. Ma, Y. Liu, Y. Liu, S. Jiang, P. Li, Y. Hao, P. Shao, A. Yin, X. Feng and B. Wang,
491 Ferrocene-linkage-facilitated charge separation in conjugated microporous polymers,
492 *Angewandte Chemie International Edition*, 2019, **58**, 4221-4226.
- 493 3. Z. Zhang, Y. Liang, H. Huang, X. Liu, Q. Li, L. Chen and D. Xu, Stable and highly efficient
494 photocatalysis with lead-free double-perovskite of Cs₂AgBiBr₆, *Angewandte Chemie
495 International Edition*, 2019, **58**, 7263-7267.
- 496 4. L. Wang, D. W. Bahnemann, L. Bian, G. Dong, J. Zhao and C. Wang, Two-dimensional
497 layered zinc silicate nanosheets with excellent photocatalytic performance for organic
498 pollutant degradation and CO₂ conversion, *Angewandte Chemie International Edition*, 2019,
499 **58**, 8103-8108.
- 500 5. L. Pan, M. Ai, C. Huang, L. Yin, X. Liu, R. Zhang, S. Wang, Z. Jiang, X. Zhang, J.-J. Zou
501 and W. Mi, Manipulating spin polarization of titanium dioxide for efficient photocatalysis,
502 *Nature Communications*, 2020, **11**, 418.
- 503 6. S. Fang, X. Lyu, T. Tong, A. I. Lim, T. Li, J. Bao and Y. H. Hu, Turning dead leaves into an
504 active multifunctional material as evaporator, photocatalyst, and bioplastic, *Nature
505 Communications*, 2023, **14**, 1203.
- 506 7. Z. Zhu, Y. Liu, C. Song, Y. Hu, G. Feng and B. Tang, Porphyrin-based two-dimensional
507 layered metal-organic framework with sono-/photocatalytic activity for water
508 decontamination, *ACS Nano*, 2022, **16**, 1346-1357.
- 509 8. Y. Wang, X. Li, S. Liu, Y. Liu, T. Kong, H. Zhang, X. Duan, C. Chen and S. Wang, Roles of
510 catalyst structure and gas surface reaction in the generation of hydroxyl radicals for
511 photocatalytic oxidation, *ACS Catalysis*, 2022, **12**, 2770-2780.
- 512 9. X. Bai, R. Zong, C. Li, D. Liu, Y. Liu and Y. Zhu, Enhancement of visible photocatalytic
513 activity via Ag@C₃N₄ core–shell plasmonic composite, *Applied Catalysis B: Environmental*,
514 2014, **147**, 82-91.

- 515 10. Y. Zhang, Y. Li and Y. Yuan, Carbon quantum dot-decorated BiOBr/Bi₂WO₆ photocatalytic
516 micromotor for environmental remediation and DFT calculation, *ACS Catalysis*, 2022, **12**,
517 13897-13909.
- 518 11. Y. Hou, F. Liu, B. Zhang and M. Tong, Thiadiazole-based covalent organic frameworks with
519 a donor-acceptor structure: modulating intermolecular charge transfer for efficient
520 photocatalytic degradation of typical emerging contaminants, *Environmental Science &*
521 *Technology*, 2022, **56**, 16303-16314.
- 522 12. L. Liccardo, M. Bordin, P. M. Sheverdyaeva, M. Belli, P. Moras, A. Vomiero and E. Moretti,
523 Surface defect engineering in colored TiO₂ hollow spheres toward efficient photocatalysis,
524 *Advanced Functional Materials*, 2023, **33**, 2212486.
- 525 13. S. Zhang, H. Lan, Y. Cui, X. An, H. Liu and J. Qu, Insight into the key role of Cr
526 intermediates in the efficient and simultaneous degradation of organic contaminants and
527 Cr(VI) reduction via g-C₃N₄-assisted photocatalysis, *Environmental Science & Technology*,
528 2022, **56**, 3552-3563.
- 529 14. Z. Zhao, P. Wang, C. Song, T. Zhang, S. Zhan and Y. Li, Enhanced interfacial electron
530 transfer by asymmetric Cu-O_v-in sites on In₂O₃ for efficient peroxymonosulfate activation,
531 *Angewandte Chemie International Edition*, 2023, **62**, e202216403.
- 532 15. C. Zhao, J. Chen, R. Zhong, D. S. Chen, J. Shi and J. Song, Oxidative-species-selective
533 materials for diagnostic and therapeutic applications, *Angewandte Chemie International*
534 *Edition*, 2021, **60**, 9804-9827.
- 535 16. Y. Gao, Z. Chen, Y. Zhu, T. Li and C. Hu, New insights into the generation of singlet oxygen
536 in the metal-free peroxymonosulfate activation process: important role of electron-deficient
537 carbon atoms, *Environmental Science & Technology*, 2020, **54**, 1232-1241.
- 538 17. Y. Nosaka and A. Y. Nosaka, Generation and detection of reactive oxygen species in
539 photocatalysis, *Chemical Reviews*, 2017, **117**, 11302-11336.
- 540 18. Y. Sheng, I. A. Abreu, D. E. Cabelli, M. J. Maroney, A.-F. Miller, M. Teixeira and J. S.
541 Valentine, Superoxide dismutases and superoxide reductases, *Chemical Reviews*, 2014, **114**,
542 3854-3918.
- 543 19. J. Lee, U. von Gunten and J. H. Kim, Persulfate-based advanced oxidation: critical
544 assessment of opportunities and roadblocks, *Environmental Science & Technology*, 2020, **54**,

545 3064-3081.

546